Journal of Geophysical Research: Oceans

RESEARCH ARTICLE
10.1029/2018JC014383

Special Section:
The Arctic: An AGU Joint Special Collection

Airborne Observations of Summer Thinning of Multiyear Sea Ice Originating From the Lincoln Sea

Benjamin A. Lange[1,2,3], Justin F. Beckers[2], J. Alec Casey[2,4], and Christian Haas[1,2,4]

[1]Alfred-Wegener-Institut Helmholtz-Zentrum für Polar- und Meeresforschung, Bremerhaven, Germany, [2]Department of Earth and Atmospheric Sciences, University of Alberta, Edmonton, Alberta, Canada, [3]Fisheries and Oceans Canada, Freshwater Institute, Winnipeg, Manitoba, Canada, [4]Department of Earth and Space Sciences and Engineering, York University, Toronto, Ontario, Canada

Abstract To better understand recent changes of Arctic sea ice thickness and extent, it is important to distinguish between the contributions of winter growth and summer melt to the sea ice mass balance. In this study we present a Lagrangian approach to quantify summer sea ice melt in which multiyear ice (MYI) floes that were surveyed by airborne electromagnetic thickness sounding within Nares Strait during summer were backtracked, using satellite imagery, to a region in close proximity (3–20 km) to spring ice thickness surveys carried out in the Lincoln Sea. Typical modal total MYI thicknesses, including ~0.4-m snow, ranged between 3.9 and 4.7 m in the Lincoln Sea during April. Ice-only modal thicknesses were between 2.2 and 3.0 m in Nares Strait during August. Total thinning including snow and ice was 1.3 ± 0.1 m including 0.4 ± 0.09 m of snow melt and 0.9 ± 0.2 m of ice melt. This translates to a seasonal net heat input of 305 ± 69 MJ/m^2 (262 ± 60 MJ/m^2 for ice only) and seasonal net heat flux of 57 ± 13 W/m^2 (45 ± 10 W/m^2 for ice only), which is unlikely to be explained by solar radiation fluxes alone. Furthermore, our approach provides an improvement on traditional ice mass balance buoy estimates because it integrates melt over larger spatial scales, where melt can be highly variable due to differential melt experienced between melt ponds, bare ice, hummocks, and ridges.

Plain Language Summary Some of the oldest and thickest sea ice remains in a small region between Canada, Greenland and the North Pole, the so-called "Last Ice Area", and will retain this ice longest into the future. Thus, continued monitoring of this unique sea ice habitat is crucial in order to document ongoing changes in the physical environment and to better predict the fate of many animals that depend on sea ice for survival (e.g., polar bears and seals). In this study, we compared sea ice thickness measurements from spring and summer to provide a better understanding of how the ice changes from season to season. Ice thickness changes provide important information on the Arctic Ocean's energy budget, a good indicator of the health of the Arctic Ocean. Our measurements are particularly important because they are the first of their kind over old, thick ice during summer in this unique region. We showed that 0.9 m of old sea ice melted from spring to summer. Although this is comparable to previous studies of old ice, it is important to continue these measurements in order document the expected ongoing changes to the sea ice environment and monitor the health of the Arctic Ocean.

Key Points:
- MYI surveyed in the Lincoln Sea during spring had modal thicknesses of 3.9-4.7 m, which thinned to 2.2-3.0 m in summer in Nares Strait
- Backtracking individual floes with satellite images was used to reconstruct positions of the same ice fields surveyed in spring and summer
- Estimated sea ice melt was 0.9 +/- 0.2 m, slightly higher than observations by ice mass balance buoys for the same region

Supporting Information:
- Supporting Information S1

Correspondence to:
B. A. Lange,
benjamin.lange@dfo-mpo-gc.ca

Citation:
Lange, B. A., Beckers, J. F., Casey, J. A., & Haas, C. (2019). Airborne observations of summer thinning of multiyear sea ice originating from the Lincoln Sea. *Journal of Geophysical Research: Oceans*, *124*, 243–266. https://doi.org/10.1029/2018JC014383

Received 27 JUL 2018
Accepted 29 NOV 2018
Accepted article online 1 DEC 2018
Published online 14 JAN 2019

1. Introduction

Arctic sea ice thickness and extent have undergone significant changes over the past ~30 years, starting with a dramatic reduction of old multiyear ice (MYI; ice that has survived one or more melt seasons) in the late 1980s and continuing into the early 1990s (Maslanik et al., 2011; Rothrock et al., 2008). This drastic reduction in thick MYI was followed by a subsequent accelerating negative trend in sea ice extent and further reduction of the perennial sea ice zone (PIZ; region of MYI; Kwok et al., 2009; Maslanik et al., 2011; Parkinson & Comiso, 2013). More recently, there is clear evidence of continued sea ice thinning throughout the Arctic (Haas et al., 2008; Lindsay & Schweiger, 2015; Meier et al., 2014). Furthermore, all regions of the Arctic have experienced an increase in melt season duration over the past few decades (Stroeve, Markus, et al., 2014).

Combining sea ice thickness observations from submarines, moorings, aircraft, and satellites showed annual mean ice thickness within the central Arctic Basin has reduced by 65% over the period 1975–2012 (Lindsay & Schweiger, 2015). One reason for the observed thinning is the flushing of large amounts of old (4+-year-old) MYI resulting in a thinner perennial ice pack that is more vulnerable to

continued thinning (Maslanik et al., 2011). Other mechanisms for thinning of perennial ice are not fully understood and require a more detailed examination of spatial and seasonal variations of Arctic sea ice thickness in order to characterize the relative contributions of the atmospheric and oceanic heat fluxes and deformation patterns on sea ice melt/growth processes to improve their representation in climate models (Massonnet et al., 2018; Stroeve, Barret, et al., 2014).

State-of-the-art climate models have substantially improved in recent years resulting in overwhelming evidence for the attribution of sea ice decline to anthropogenic forcing (Intergovernmental Panel on Climate Change, 2013; Stroeve et al., 2012). However, there remains large variability within and between these climate model projections of sea ice decline (Intergovernmental Panel on Climate Change, 2013; Massonnet et al., 2012; Stroeve et al., 2012). Reasons for this persisting uncertainty remain contested (Massonnet et al., 2012; Notz, 2015; Rosenblum & Eisenman, 2017). A recent study by Massonnet et al. (2018) indicated that improved sea ice thickness observations and reduced sea ice thickness biases are key to improving sea ice projections. Furthermore, the spatial distribution of sea ice thickness is a well-known factor having a crucial impact on future changes to Arctic sea ice extent and volume (Stroeve, Barrett, et al., 2014).

One important aspect of sea ice thickness is its large seasonal variation. Quantifying not only the mean state but the seasonal ice thickness cycle provides important insights into the regional, seasonal, and interannual variability of atmospheric and oceanic forcing, which is directly related to sea ice mass balance (Perovich & Richter-Menge, 2015; Perovich et al., 2014). Due to the large financial costs and logistical difficulties of operating long term ice stations, there are few results documenting the seasonal cycle of ice thickness for the Arctic Ocean. Deployments of ice mass balance buoys (IMB) are currently the most effective and widely used method to monitor seasonal and annual sea ice mass balance changes with particular improvements in the spatial coverage of IMB deployments/observations within the PIZ over the past 10 years (Perovich & Richter-Menge, 2015). Based on over 50 years of observations within the Arctic Ocean, Perovich and Richter-Menge (2015) demonstrated that there was large regional and temporal variability in bottom and surface melt ranging between 0.16 and 2.94 m. IMB observations, however, represent a single point location; therefore, the observed melt rates may not capture the floe-scale (hundreds of meters) to regional-scale variability (tens of kilometers) of melt processes, which are largely controlled by snow and ice morphology and local feedback processes. Drill-hole measurements show that the horizontal scales of variability of snow and ice thickness of MYI in the Lincoln Sea ranges between 9 and 25 m and 14 to 24 m, respectively (Lange et al., 2017). The variability of sea ice thickness and surface topography of an undeformed MYI floe is largely the result of differential melt and freezing experienced over the life of the MYI floe. Thus, we need to capture the floe-scale spatial variability of melt processes in order to provide accurate estimates of the seasonal ice thickness cycle.

Seasonal ice thickness observations are also required in order to make sea ice volume flux estimates (e.g., Kwok, 2005; Kwok et al., 2010). Sea ice volume fluxes from the Canadian Arctic Archipelago (CAA) are important in terms of the hydrography in Baffin Bay with potential ecological and climatic implications. However, there is large variability in the annual sea ice volume flux estimates coming from the CAA, with estimates ranging from 500 to 870 km^3 (Cuny et al., 2005; Tang et al., 2004). The proportional contributions from the different gateways within the CAA also have high variability. Annual sea ice volume flux estimates from Nares Strait range from 33 km^3 in years when sea ice export is inhibited by the formation of an ice arch in Nares Strait up to 254 km^3 during years when an ice arch does not form (Kwok et al., 2010). Kwok (2005) suggested that refining ice volume estimates could be accomplished by improving ice drift and sea ice thickness observations within Nares Strait. This has partially been fulfilled by Kwok et al. (2010) who used a combination of imaging and altimetric satellite remote sensing observations. However, due to the fact that ICESat ice thickness observations stopped in 2008 (Kwok, 2010) and CryoSat-2 only commenced in 2010 (Laxon et al., 2013), there is a gap in satellite-based ice volume flux observations in Nares Strait in 2009.

The Lincoln Sea/Nares Strait study region is important for four reasons: (1) the thickest ice in the Arctic resides in the Lincoln Sea, and it will likely be home to the last remaining amounts of MYI in the near future (Haas et al., 2017, 2006, 2010); (2) large volumes of sea ice and freshwater are exported from the Arctic Ocean via Nares Strait (Kwok et al., 2010); (3) The large volume of very thick (>3 m) MYI advected through Nares Strait poses a potential hazard for shipping and offshore activities farther south and within the Northwest Passage (Barber et al., 2018; Haas & Howell, 2015); and (4) the export of freshwater and sea ice has ecological implications for regions downstream (Rasmussen et al., 2011).

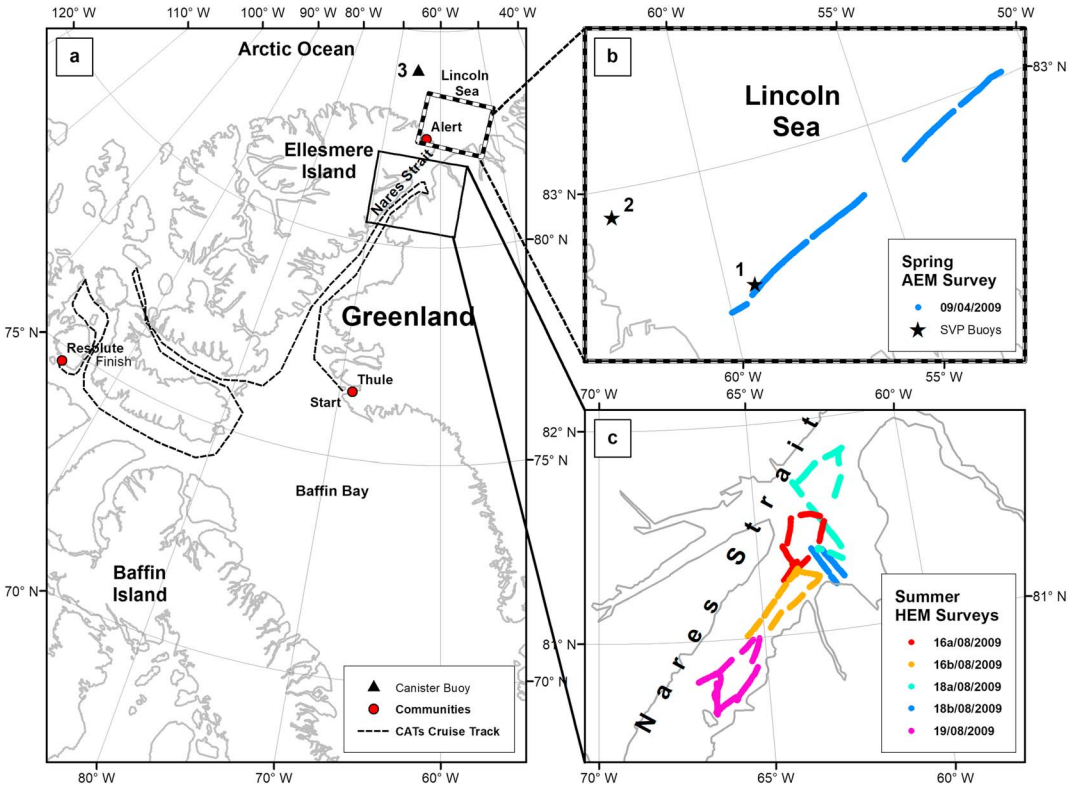

Figure 1. Maps of (a) the Eastern Canadian Arctic Archipelago and Western Greenland showing the Canadian Arctic Through flow (CATs) cruise track and canister buoy deployment location, (b) zoomed in region of the Lincoln Sea showing the AEM survey and two SVP buoy deployment locations during spring 2009, and (c) zoomed in region of northern Nares Strait showing HEM surveys conducted during the summer CATs cruise. AEM = airborne electromagnetic; HEM = helicopter-borne electromagnetic; SVP = Surface Velocity Program.

To the best of our knowledge, this study presents the first comparison of spring and summer airborne electromagnetic (AEM) sea ice thickness surveys conducted over MYI originating from the same region. This data set represents an important contribution to the characterization of the annual cycle of sea ice thickness in the Lincoln Sea and Nares Strait. AEM total (snow plus ice) thickness observations were conducted over MYI in the Lincoln Sea during April 2009 and ice-only thickness observations were conducted in Nares Strait during August 2009. We describe the summer ice conditions in Nares Strait and characterize the thinning of ice and snow that has taken place as the MYI drifted from the Lincoln Sea in April into Nares Strait in August. We applied a Lagrangian approach by surveying sea ice from the same region by tracking individual ice floes with satellite data. This is opposed to an Eulerian approach when surveys of the same region are carried out but where the ice was likely replaced. To better distinguish between melting of different ice types, we also extracted level ice areas from the profiles and analyzed them separately from the complete profiles.

2. Data and Methods

2.1. Measurements

2.1.1. Airborne EM Ice Thickness Surveys

Fixed-wing AEM total (snow plus sea ice) thickness surveys were conducted in the Lincoln Sea during spring 2009 and helicopter-borne electromagnetic (EM) surveys of ice (snow was melted) thickness in Nares Strait during summer 2009. More information on methodological aspects of AEM measurements is given below. The spring Lincoln Sea survey was carried out with a DC3-T airplane on April 9 and was conducted over stationary sea ice, with little open water in the surveyed areas (Haas et al., 2010). The AEM survey on 9 April, 2009 (Figure 1 in Haas et al., 2010) was subdivided into continuous profiles based on breaks in the AEM data acquisition with a goal to maintain profile lengths of 10 to 20 km (Figures 1 and 2). This profile

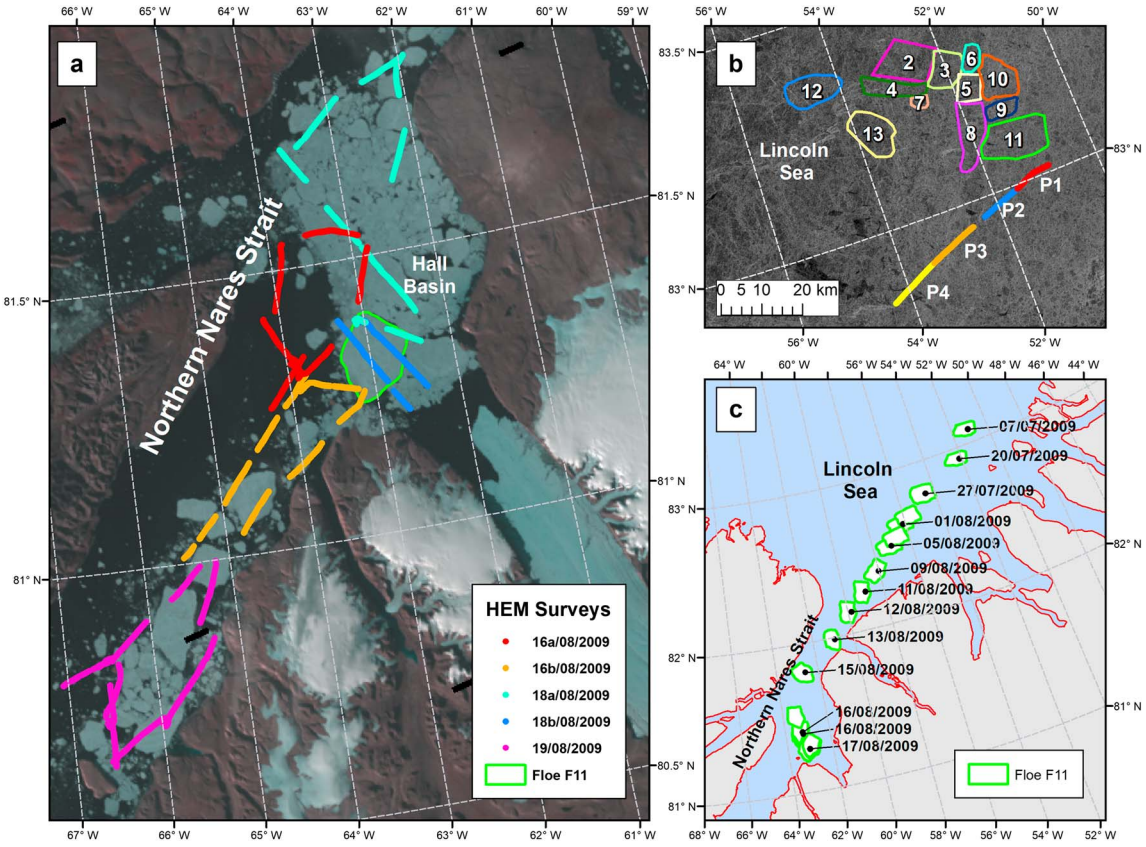

Figure 2. Illustration of AEM flights and floe tracking. (a) Moderate Resolution Imaging Spectroradiometer image of northern Nares Strait and Hall Basin overlaid with the summer HEM survey tracks and the outline of floe F11 (image acquisition date 18 August 2009). (b) Phased Array type L-band synthetic aperture radar image (acquired 17 April 2009) of the Lincoln Sea overlaid with the spring AEM subprofile tracks and the winter freeze-in locations of the backtracked floes including F11. (c) Map of northern Nares Strait and the Lincoln Sea showing the backtracked locations of floe F11. AEM = airborne electromagnetic; HEM = helicopter-borne electromagnetic.

length was chosen in order to capture regional variations in sea ice thickness (different ice regimes) in addition to maintaining a consistent profile length to the summer helicopter-borne EM (HEM) survey lengths over individual floes. Only profiles near the ice that was also surveyed in summer were used for comparison. The resulting profiles are depicted in Figure 2b.

The summer Nares Strait surveys were carried out by a helicopter onboard the Canadian Coast Guard Ship Henry Larsen between 16 and 19 August 2009, during the Canadian Arctic Through-flow (CATs) cruise. These HEM surveys were conducted over rapidly drifting sea ice (~1 m/s), with large regions of open water and brash ice within the survey areas (Figure 2). It must be noted that we had no chance in the summer to carry out our dedicated surveys over the exact same sea ice surveyed in spring. This was the result of, first, the ice marked by buoys deployed on the sea ice in spring had either already drifted south through Nares Strait or was still in the Lincoln Sea at the time of summer surveys. Second, the cruise plan, logistics, and weather conditions did not allow specific, dedicated surveys. Third, we had no access to near-real-time satellite data during the cruise to inform our survey planning.

Five HEM survey flights were conducted in Nares Strait during the CATs cruise. These surveys were used for quantifying the summer ice thickness of the sea ice floes tracked from the Lincoln Sea. Areas of open water were common in these surveys. The open water regions were used to confirm the calibration of the HEM measurements, as their thickness should be 0 m. The accuracy of the measurements was checked by ensuring distinct narrow peaks (width ± 0.1 m corresponding to expected instrument noise) were present at ~0 m of the ice thickness distributions.

The summer HEM surveys were segmented into short profiles because there is a lot of brash ice in summer, the thickness of which cannot be measured accurately using the EM, and because smaller floes and brash ice

melt faster (due to their larger surface area to volume ratio) so that their thickness cannot be compared as well as that of large floes. To segment the summer surveys by ice floe, the HEM data were first loaded into ArcMap with coincident or near-coincident (e.g., within 2 hr) satellite images. The HEM surveys were examined with delineated floe outlines and satellite images to determine the floe edges within the HEM surveys. Once the floe edges were identified in the HEM ice thickness profiles, the regions corresponding to that floe were extracted and named according to the corresponding floe ID, profile number (e.g., multiple profiles were conducted over the same floes), and survey date and time.

Furthermore, the inclusion of EM ice thickness measurements near floe edges could result in an underestimation of ice thickness because sea ice experiences enhanced melt along the perimeter of floes (Perovich et al., 2003) and because open water adjacent to the floes but within the large EM footprint would contaminate the ice thickness retrievals (see below). Therefore, we applied "edge exclusions" to the surveys, meaning that measurements that were conducted within 100 m of a floe edge were not included in the final ice thickness analysis.

A detailed description of the AEM instrument and data processing is provided in Haas et al. (2009); thus, we only provide a brief summary of the EM method in this section. In addition to the EM electronic components, the AEM system also includes a vertically downward looking single beam laser altimeter. The EM measurements are sampled at 10 Hz and the laser altimeter at 100 Hz. The resulting point spacing depends on the flying speed, which was 50 m/s for the airplane and 30 m/s for the helicopter, corresponding to EM and laser point spacing of 5 m (EM) and 0.5 m (laser), and 3 m and 0.3 m, respectively. The difference in airplane and helicopter speed does not affect the processing of the EM measurements and therefore results remain consistent with procedures outlined in Haas et al. (2009).

The footprint of the EM instrument is about 3.7–3.8 times the height of the instrument above the water (i.e., ice-water interface; Kovacs et al., 1995; Reid et al., 2006). Given typical laser altimeter readings of 12.5 to 20 m above the snow/ice surface, combined with a dominant modal total thickness of 3 to 4 m, this corresponds to EM footprints with radii between ~30 and 45 m.

The EM measurements have an accuracy of ±0.1 m over level ice (Haas et al., 2009; Pfaffling et al., 2007); however, estimates are less reliable over ridges due to the geometry and structure of deformed ice. The conductive nature of ridge keels causes induction of a secondary field within the keel (Reid et al., 2006). Deformed ice thickness observations are further complicated by the fact that the EM footprint can be larger than the width of the ridge keel and will induce secondary fields in the water surrounding the keel (Reid et al., 2006). These two factors can result in the underestimation of maximum ridge thickness by as much as 50% (Haas & Jochmann, 2003). The potential inaccuracies introduced to the total thickness (spring) or ice thickness (summer) calculations by rough, deformed ice were accounted for by analyzing representative level ice regions separately.

When comparing the spring total thickness and summer ice thickness survey results, it is also important to note that EM measurements represent estimates of total, ice plus snow thickness, because both ice and snow are highly resistive and cannot be distinguished electromagnetically. Here we use independent in situ snow observations acquired during spring to evaluate the contribution of snow depth to total thickness measurements, and the amount of snow melting. In the summer, all snow had melted and the EM retrievals represent only ice thickness.

Furthermore, we evaluated the statistical reliability of surface roughness (e.g., root-mean-square [rms] height, see section 2.1.3), modal thickness, and mean thickness estimates for different profile lengths (from 50 to 50,000 m) by calculating the standard error (SE). The profile lengths were calculated as the cumulative distance by combining different subprofiles and excluding the gaps and edge exclusions. The cumulative profile distance for level ice excludes ridges and the surrounding buffer zone. The SE is the standard deviation of an ensemble of mean rms values, modal thicknesses, or mean thicknesses obtained from profile subsections of the same length, which all come from the same larger profile. We calculated SE following Wadhams (1997) and Rabenstein et al. (2010). We evaluated the statistical reliability of the profile lengths using a percent SE threshold of 12.75% according to Wadhams (1997). The percent SE is the percent of the SE relative to the rms, modal thickness, or mean thickness of the entire profile. Above this threshold values the profile length was considered to have significant spatial variability (Wadhams, 1997).

2.1.2. In Situ Measurements

After completion of the April 2009 AEM surveys a helicopter was used to land on the ice in the study region to carry out snow thickness measurements with a ruler stick (Haas & Druckenmiller, 2009) and to deploy three buoys. We deployed two MetOcean ice Surface Velocity Program (SVP; Figure 1b) buoys that measure hourly GPS positions and the sea ice surface temperature. The third buoy, a MetOcean canister buoy with an air temperature sensor on a mast approximately 2 m high, was deployed farther north than the SVPs (Figure 1a).

To estimate the ice thickness of the spring surveys, we subtracted the modal snow thickness of 0.42 m (sd ± 0.18 m; N = 1212) determined from in situ surveys of snow depth measurements from a total of six MYI sites in the Lincoln Sea (Lange et al., 2017).

2.1.3. Laser Altimeter Surface Roughness and Ridge Surveys

Laser altimeter measurements were used to discriminate between level and deformed ice and to observe estimates of surface roughness for comparison with satellite radar backscatter signatures. The EM instrument measured the distance of the EM bird above the ice/snow surface using an onboard Riegl LD90-3100Hs laser altimeter operating at a wavelength of 905 nm with an accuracy of 2.5 cm. Low-frequency aircraft altitude variations were removed from the laser data using a three step filter process described in detail by Hibler (1972). The derived surface elevation values are not identical to freeboard but are elevation changes relative to the adjacent level ice surface (see also Beckers et al., 2015; Fors et al., 2016). From the resulting laser-derived surface elevation profiles we calculated the rms height, a common measure of surface roughness (Manninen, 1997).

2.1.4. Level Ice Extraction

In addition to analyzing complete thickness profiles, we also extracted and analyzed profile sections of only the level ice because (i) the EM thickness estimates have increased uncertainty over deformed, ridged sea ice due to the unconsolidated, porous, and conductive nature of this type of ice (Haas et al., 2009); (ii) level ice melt rates are more representative of thermodynamic processes than those over ridges because ridges are largely dependent on dynamic atmospheric and oceanic processes; and (iii) in the thickness distributions of complete profiles, smaller ridges formed within thinner ice contribute samples to the modal thickness of thicker, level ice, and could therefore result in the misrepresentation of the dominant level ice class (Haas, 2010; Thorndike et al., 1975).

First, ridge sail locations were identified in the surface elevation data. Ridges were defined as local maxima of the surface elevation profiles exceeding a threshold height of 0.80 m above the reference level ice, consistent with previous work done over MYI by, for example, Beckers et al. (2015), Rabenstein et al. (2010), and von Saldern et al. (2006). Neighboring ridges also had to satisfy a Rayleigh criterion: They had to be separated by a trough at least half their vertical height to be identified as separate features.

Level ice regions were then extracted from the EM profiles by applying a 40 m buffer (radius) to the ridges identified in the laser elevation profiles. The level ice regions may comprise a mixture of first-year ice (FYI) and MYI in spring but only MYI in summer. This is because the thinner, melt ponded FYI is easily smashed into rubble ice during the export into Nares Strait, and thus, no large FYI floes survive this process (see time series of satellite imagery in Appendix B of Lange, 2012). A 40-m buffer was chosen because with an instrument footprint radius between 30 and 45 m any influence of a ridge on level ice thickness estimates should have been eliminated. Thickness measurements outside of the 40-m buffer regions were selected and extracted from the data to represent level ice regions. However, it should be noted that this definition of level ice still allows significant elevation and thickness variability with surface undulations less than 0.8 m high, for example, the presence of hummocks. In addition, due to strong surface melt of MYI, the ice surface can appear relatively level, while there can still be strong bottom topography underneath (e.g., Haas et al., 2017).

2.2. Satellite Imagery

Satellite imagery was used to backtrack individual ice floes from Nares Strait to the Lincoln Sea and to classify ice regimes in the Lincoln Sea. We used a time series consisting of 109 synthetic aperture radar (SAR) images and 121 Moderate Resolution Imaging Spectroradiometer (MODIS) optical images for these tasks (for a full set of satellite images refer to Appendix B in Lange, 2012). In addition, we used backscatter changes from the Advanced Scatterometer (ASCAT) flown onboard the European Meteorological Operational satellite program (MetOp-A) to observe the timing of melt onset in the study region.

2.2.1. SAR Imagery

Backtracking was done with ENVISAT Advanced SAR (ASAR) imagery. ASAR is a C-band active microwave instrument operating at 5.3 GHz (wavelength ~5 cm; European Space Agency, 2007). The ASAR data set includes both Image Mode medium-resolution and Wide Swath Mode medium-resolution products. Both products have a spatial resolution of 150 × 150 m. The Wide Swath Mode data provided better spatial and temporal coverage of the study region so they comprise the majority of the ASAR data set.

The ASAR images were georeferenced using built-in functions in ENVI v4.3. All images demonstrated accurate georeferencing with no or very little (<500 m) deviation from the Global Self-Consistent, Hierarchical, High-Resolution Geography coastline.

ASAR images used for tracking floes were not calibrated as quantitative backscatter analyses were not conducted with these images.

In addition to ASAR imagery, one image from the Japanese Phased Array type L-band SAR (PALSAR) acquired in April was used to classify the sea ice into rough and very rough ice, as a proxy for ice thickness. The data were calibrated and georeferenced using Alaska Satellite Facility MapReady software. The calibrated image was exported in Geotiff file format and demonstrated accurate geolocation in ArcMap when compared to the outline map and other ASAR images processed using ENVI. Backscatter values were extracted along two transects that crossed the tracked floes' spring freeze-in locations in the Lincoln Sea and along the full AEM profile. Trend analyses were conducted on the transect backscatter values in order to determine any patterns or gradients within this region and to determine any correlations between backscatter and total thickness or surface roughness (rms). For each PALSAR pixel along the AEM profile, we calculated the mean of all total thickness observations and rms of all surface elevation measurements found within each corresponding pixel.

On average, there were two ASAR image acquisitions per day near the study region. Many of the images, however, did not have adequate coverage of the study site to be useful. There were also occasional temporal gaps in the ASAR data set of up to 3 days. Therefore, a complementary data set of MODIS imagery was included to fill the temporal gaps during the rapidly changing ice conditions in the study region observed in summer.

2.2.2. MODIS Imagery

ASAR images were supplemented by images acquired from the MODIS (King et al., 2004; National Aeronautics and Space Administration, 2012). For the period 5 July to 13 August 2009, we acquired an average of two images per day. During the period 14 to 19 August 2009, better temporal coverage was required because this is when the surveyed ice floes entered Nares Strait and began to break up and drift rapidly. Complete temporal coverage was also required to ensure HEM surveys had coincident satellite images to help define the HEM profile for each floe.

We used only bands 1 and 2 because they had the highest spatial resolution (250 m). At these wavelengths (645 and 857 nm), reflected energy is unable to penetrate through clouds, resulting in many unusable images. However, there were sufficient usable MODIS acquisitions, in conjunction with the ASAR data, to track the HEM-surveyed sea ice floes back to the Lincoln Sea. The MODIS images also helped to discriminate between snow/ice and open water; this reduced uncertainty in the interpretation of the ASAR data during high wind conditions when wind-roughened water and sea ice can be difficult to discriminate in SAR images.

MODIS images were processed using ENVI/IDL script-based functions to automate the processing of MODIS imagery. Processing of MODIS imagery in ENVI required "bowtie correction," which geolocated the image to the pixel's center coordinates and accounted for the fact that the pixels near the edge of the swath are larger than those at nadir. The MODIS images were exported using a standard ENVI file format compatible with ArcMap. Two hundred thirty images were imported into ArcMap and quality checked for accurate geolocation by comparing them to the high resolution coastline and ASAR images.

2.2.3. ASCAT Data

ASCAT data were obtained from National Aeronautics and Space Administration's Scatterometer Climate Record Pathfinder at Brigham Young University (Lindsley & Long, 2010) to determine the onset of melt. ASCAT is a C-band scatterometer operating at 5.255 GHz, and the scatterometer image reconstruction data product used in this study has a pixel spacing of 4.45 km. Daily backscatter maps are derived from

multiple passes in order to provide enhanced spatial coverage and spatial resolution. The used data product was an average over two consecutive days of data with an overlap of one day.

2.3. Sea Ice Floe Tracking, Drift Speed, and Volume

As the ice surveyed in April in the Lincoln Sea had already drifted past the study region in Nares Strait in August and could not be surveyed any more, we used a reverse approach of ice floe backtracking to confirm that the floes surveyed in summer originated from the vicinity of the floes surveyed in spring. We surveyed 13 different ice floes in summer. Of those 13 floes it was possible to successfully backtrack only 12 floes to their winter freeze-in locations. Of these 12 floes only 11 floes had sufficient airborne survey observations to compare the HEM ice thickness surveys in summer with the AEM total thickness surveys in spring. Backtracking was conducted by first identifying the floes that were surveyed in Nares Strait during the summer CATs cruise. The HEM survey tracks were overlaid with the entire data set of ASAR and MODIS images in ArcMap. For each HEM survey, several coincident (or near coincident) images were used to accurately identify the surveyed floes. Each floe was assigned a unique ID (e.g., F01, F02, … F13) and digitized to create a polygon shapefile in ArcMap v10.2.

The largest and most uniquely shaped floes were tracked first as they were the easiest to follow from image to image, even with large temporal gaps. Many small floes could not be tracked because of the similarity between the shape and size of these floes, and the temporal coverage was not sufficient to maintain confidence in the consistent identification of the same smaller sized floes. Once the floes were identified and named, the floes were backtracked by keeping the floe polygon layers visible and looking at the previous image (earlier in time). Each floe was again identified, named, and outlined from that previous image. Floes were identified and outlined in each previous image until the floe was stationary in the ice pack and had reached its winter origin (i.e., its location of freeze-in during the previous fall/winter). Most floes that entered Nares Strait from the Lincoln Sea were large and broke into smaller pieces. When backtracking these floe breakup events, the floes combined into larger floes. During floe amalgamation, the original floe outline was maintained, as much as possible, as part of the larger floe.

Average drift speed in meters per second was calculated for each floe by measuring the distance (m) from the centroid of the floes at their most northern location within Nares Strait compared to the centroid of the floes at the most southern locations within Nares Strait, divided by the total time elapsed in seconds between these two locations. Ice floes were stationary in the Lincoln Sea from the time of the spring survey up to the ice arch failed on 6 July. Even after the ice arch failed ice floes lingered in the Lincoln Sea with very little movement between 6 July and 1 August (Figure 2c), which would have substantially influenced (decreased) average drift speed over that period. For this reason and to maintain comparability with other studies measuring drift and fluxes in Nares Strait (e.g., Kwok, 2005; Kwok et al., 2010), we measured drift only from the point the floes entered Nares Strait. Area (km^2) was calculated from the outlined floes using ArcMap's built-in shapefile polygon area calculator. We then took an average of all polygon outlines for each corresponding floe to assign a single mean area to each floe. Floe volumes in cubic kilometers were subsequently calculated as the area (km^2) multiplied by the mean ice thickness (km) of the floe.

2.4. Sea Ice Melt and Energy Budget

In order to determine melt onset, ASCAT images were analyzed in conjunction with temperature data from the three drifting buoys deployed in May. Melt onset was estimated from the buoy data based on the identification of rapid increases in temperature to around or above 0 °C. In addition, melt onset and the date when snow was completely melted from the sea ice surface were observed from time series of ASCAT data based on transitions in backscatter intensity. ASCAT backscatter intensity is dependent on surface properties of the snow and ice. Melt onset is characterized by a shift from high to low backscatter due to the presence of liquid water in the snow, which causes absorption of the incident microwaves within the snow pack and masks the backscatter signature of the underlying ice (Mortin et al., 2014). Once the snow has melted, the disappearance of wet snow, the reduction of liquid water content within hummocks, and the presence of bare ice and wind-roughened melt ponds cause a transition from low backscatter to high backscatter (Mortin et al., 2014).

We computed a summer energy budget estimate using the thinning of the snow and ice as measured by the spring and summer EM surveys. The total amount of sea ice and snow melted between the survey dates of 9

Table 1
Summary of the 13 Backtracked Sea Ice Floes, Including Mean Drift Speed and Floe Area, Mean Floe Ice Thickness, and Floe Ice Volume in August 2009

Floe ID	Date/time north location (DD/MM/YYYY HH:MM (UTC))	Date/time south location (DD/MM/YYYY HH:MM (UTC))	Time interval (s)	Drift speed (summer; m/s)	Floe area (summer; km^2)	Mean floe ice thickness (summer; m)	Floe ice volume (summer; km^3)
F01[a]	15/08/2009 4:51 p.m.	19/08/2009 5:10 p.m.	346,740	0.27	14.22	3.6	0.05
F02	11/08/2009 3:42 p.m.	19/08/2009 5:10 p.m.	696,480	0.23	103.96	3.7	0.39
F03	15/08/2009 8:50 p.m.	19/08/2009 5:10 p.m.	332,400	0.17	57.64	3.1	0.18
F04	11/08/2009 3:42 p.m. -	16/08/2009 11:10 p.m.	458,880	0.21	43.47	3.9	0.17
F05	13/08/2009 1:15 a.m.	16/08/2009 11:10 p.m.	338,100	0.30	22.74	2.8	0.06
F06	13/08/2009 4:35 p.m.	16/08/2009 11:10 p.m.	282,900	0.28	19.41	3.7	0.07
F07	11/08/2009 3:42 p.m. -	16/08/2009 11:10 p.m.	458,880	0.21	7.77	3.4	0.03
F08	13/08/2009 4:35 p.m.	18/08/2009 5:10 p.m.	434,100	0.17	101.94	4.5	0.46
F09	13/08/2009 4:35 p.m.	19/08/2009 3:10 p.m.	513,300	0.25	30.63	4.1	0.13
F10	15/08/2009 11:30 a.m.	19/08/2009 11:40 p.m.	389,400	0.22	76.66	3.8	0.29
F11	12/08/2009 4:51 p.m.	18/08/2009 7:45 p.m.	528,840	0.20	167.50	3.5	0.59
F12	13/08/2009 9:05 p.m.	18/08/2009 5:10 p.m.	417,900	0.19	74.51	4.0	0.30
F13[b]	09/08/2009 4:45 p.m.	19/08/2009 11:40 p.m.	888,900	0.23	75.89	—	—

[a]Floe could not be backtracked to its winter freeze-in location in the Lincoln Sea due to insufficient satellite data for the ice conditions (e.g., cloud cover, rapid ice drift, and rapid breakup of ice floes). These results represent drift from northern extent of tracking within Nares Strait. [b]Insufficient airborne survey data.

April and 18 August 2009 was used to calculate a seasonal, total net heat ($\boldsymbol{Q_t}$) following Perovich et al. (2003) in the form:

$$\boldsymbol{Q_t} = \boldsymbol{Qi} + \boldsymbol{Qs} = (\rho_i\, \Delta \boldsymbol{H_i} + \rho_s\, \Delta \boldsymbol{H_s})\, \boldsymbol{L_f} \tag{1}$$

where Q_i is the net heat of melting sea ice, Q_s the net heat of melting snow, $\boldsymbol{\rho_i}$ is the density of sea ice (900 kg/m^3), $\boldsymbol{\rho_s}$ the density of snow (280 kg/m^3; Lange et al., 2015), $\boldsymbol{\Delta H_i}$ is change in ice thickness, $\boldsymbol{\Delta H_s}$ the change in snow thickness, and $\boldsymbol{L_f}$ is the latent heat of fusion of ice and snow (0.335 MJ/kg). The seasonal net heat flux ($\boldsymbol{F_{net}}$) was calculated following Perovich et al. (2003) in the form

$$\boldsymbol{F_{net,i}} = {}^{\boldsymbol{Q_i}}\!/_{\boldsymbol{\Delta t}} \tag{2}$$

where $\boldsymbol{Q_i}$ (or substituted for $\boldsymbol{Q_s}$) is calculated by modifying equation (1) to calculate $\boldsymbol{Q_i}$ (ice only) or $\boldsymbol{Q_s}$ (snow only). $\boldsymbol{\Delta t}$ is either the time interval (in seconds) between melt onset and summer survey for ice melt ($F_{\mathrm{net},i}$ of sea ice), or between onset of melt and the ASCAT-derived day when most of the snow was absent ($F_{\mathrm{net},s}$ snow). $\boldsymbol{F_{net}}$ is then the sum of $\boldsymbol{F_{net,i}}$ and $\boldsymbol{F_{net,s}}$.

3. Results

3.1. Sea Ice Conditions and Drift From April to August 2009

During the winter of 2009, sea ice export through Nares Strait was inhibited by the formation of a stable ice arch in the Lincoln Sea that spanned the opening into Nares Strait until 6 July (for a full set of satellite images refer to Appendix B in Lange, 2012). Between this date and the summer HEM survey dates, a total of 13 ice floes was backtracked, of which only 12 floes (F02 to F13) could be backtracked to their freeze-in locations within a relatively small region in the Lincoln Sea (approximate dimensions: 70 by 35 km; Figure 1b). Of these 12 floes, only 1 (F13) was excluded from further analyses due to insufficient airborne survey coverage.

The tracked sea ice floe positions and the times of the image acquisitions are displayed in Supporting Information Figures S1 and S2 in the supporting information. Many floes have large spatial gaps in the drift tracks, as many originated from a larger common floe. The winter freeze-in locations of the 12 tracked floes are shown in Figure 1b. From the winter freeze-in to 6 July, the sea ice was immobile. The cumulative floe drift distances (from entering Nares Strait to surveyed locations) ranged between ~75 and 205 km during the period from 6 July, when the ice arch broke up, to 16–19 August 2009, the dates of summer HEM surveys. When considering only backtracked positions within Nares Strait, the mean drift speed for all floes was 0.23 m/s with individual ice floe drift speeds ranging from 0.17 to 0.30 m/s (Table 1). The surveyed floes had areas

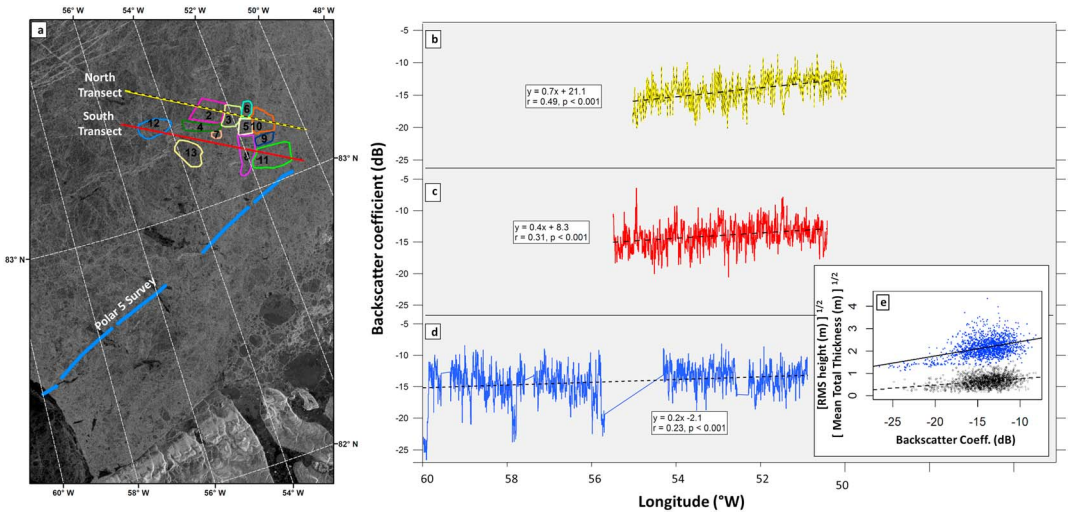

Figure 3. (a) Phased Array type L-band synthetic aperture radar image (acquired 17 April 2009) of the Lincoln Sea showing backtracked floe locations during spring and the transects used to extract backscatter values. Extracted backscatter profiles are shown for (b) the north transect (black and yellow lines), (c) the south transect (red lines), and (d) the Polar 5 survey (blue lines). Legends in (b)–(d) show ordinary least squares linear trend lines (stippled lines) and correlation coefficients *r*. (e) Square root transformed rms (black) and total thickness (blue) along Polar 5 survey line versus extracted backscatter values from corresponding pixels with trend lines. rms = root-mean-square.

ranging between ~8 and 170 km^2, mean ice thicknesses ranging between 2.8 and 4.5 m, and corresponding ice volume estimates ranging between 0.03 and 0.59 km^3 (Table 1).

3.2. Lincoln Sea Backscatter and Surface Roughness Variability

To characterize ice conditions along the spring AEM survey in the Lincoln Sea, we examined gradients in radar backscatter in the 17 April 2009 ALOS PALSAR image (Figure 3a). Backscatter values were extracted along two transects that intersect the freeze-in locations of the 12 backtracked floes (Figure 3a). The extracted backscatter profiles for the north and south transects are shown in Figures 3b and 3c. Along both transects, significant weak to moderate longitudinal backscatter trends were observed with backscatter increasing from west to east. Correlation coefficients were $r = 0.49$ ($p < 0.01$) and $r = 0.31$ ($p < 0.01$) were observed for the north and south transects, respectively. A weak but significant trend ($r = 0.23$, $p < 0.01$) was also observed along the entire AEM profile length (Figures 3a and 3d). Past studies have demonstrated that L-band SAR sensors are highly sensitive to ridged sea ice and, compared to C-band SAR sensors, are less sensitive to volume scattering from air bubbles in MYI (Casey et al., 2016; Dierking & Busche, 2006; Dierking & Dall, 2007). We observed weak but significant positive correlations between square root transformed mean total thickness per PALSAR pixel and backscatter ($r = 0.35$, $p < 0.01$; Figure 3e) and between square root transformed rms per pixel and backscatter ($r = 0.28$, $p < 0.01$; Figure 3e). Therefore, we attribute the variability in backscatter along these transects to changes in sea ice surface roughness and total thickness, from lower surface roughness and thinner ice in the west to higher surface roughness and thicker ice in the east (Figure 3a).

Laser derived rms heights of the four subprofiles P1–P4 in the Lincoln Sea ranged between 0.54 and 0.69 m, with an overall average of 0.62 m for all subprofiles combined (Table 2). Laser derived rms heights for the summer floe profiles in Nares Strait were all smaller than the spring observations with a range between 0.34 and 0.43 m and a mean of 0.37 m for all floes (Table 2). This large difference is likely due to the fact that winter profiles included a larger fraction of ridge/rubble fields of unconsolidated sea ice comprising ~72% of the spring survey and during ice breakup a larger portion of those ridges broke off and collapsed and formed brash ice regions, which melt faster due to increased surface area. Ridged ice only made up ~58% of the sea ice coverage in summer.

3.3. Sea Ice Thickness

3.3.1. Spring Total Thickness in the Lincoln Sea

The full spring AEM survey included 21,491 total (snow plus ice) thickness measurements from 107 km of ground coverage (Figure 2b). During the spring survey there was no open water to confirm the accuracy

Table 2
Summary of Thickness and Surface Roughness (rms) Results for All Surveys Individually and Summarized by Season

Season	Survey	Modal thickness (m)			Mean thickness ± sd (m)			rms height (m)
		Complete (length in kilometers)	Level ice (length in kilometers)	Difference	Complete	Level ice	Difference	
Spring	P1	**4.7 (10)**	3.6 (4)	1.1	**5.5 ± 2.2**	4.7 ± 1.5	0.8	0.54
(Total thickness)	P2	**3.9 (11)**	3.6 (6)	0.3	**5.0 ± 1.8**	4.4 ± 1.4	0.6	0.55
	P3	**4.1 (13)**	3.8 (4)	0.3	**5.8 ± 2.2**	4.8 ± 1.8	1.0	0.69
	P4	**4.3 (15)**	4.5 (4)	−0.2	**5.1 ± 1.7**	4.3 ± 1.1	0.8	**0.58**
	All	**3.9 (49)**	**3.7 (18)**	0.2	**5.3 ± 2.0**	**4.5 ± 1.5**	0.8	**0.62**
Summer	F01	**2.5 (100)**	**2.5 (47)**	0.0	**3.6 ± 1.5**	**3.0 ± 1.1**	0.6	**0.35**
(Ice thickness)	F02	2.5 (8)	2.4 (5)	0.1	3.7 ± 1.6	**3.1 ± 1.1**	0.6	0.38
	F03	2.2 (19)	2.1 (14)	0.1	**3.1 ± 1.2**	**2.8 ± 1.1**	0.3	**0.35**
	F04	2.7 (4)	2.6 (3)	0.1	3.9 ± 1.6	3.2 ± 0.9	0.7	0.35
	F05	2.4 (13)	2.4 (9)	0.0	**2.8 ± 0.9**	**2.7 ± 0.8**	0.1	0.34
	F06	2.6 (25)	2.5 (12)	0.1	**3.8 ± 1.5**	**3.0 ± 1.1**	0.8	**0.39**
	F07	2.4 (3)	2.5 (2)	−0.1	3.4 ± 1.3	2.6 ± 0.9	0.8	0.42
	F08	3.6 (13)	2.9 (4)	0.7	**4.5 ± 1.8**	3.6 ± 1.4	0.9	0.41
	F09	3.8 (4)	2.6 (1)	1.2	4.1 ± 1.4	3.5 ± 1.2	0.6	0.43
	F10	2.7 (8)	2.6 (4)	0.1	3.8 ± 1.4	3.3 ± 1.1	0.5	0.37
	F11	**3.5 (64)**	**2.3 (19)**	1.2	**3.5 ± 1.5**	**2.9 ± 1.2**	0.6	**0.41**
	F12	3.0 (5)	3.0 (3)	0.0	4.0 ± 1.7	3.3 ± 1.1	0.7	0.34
	All	**2.5 (266)**	**2.4 (123)**	0.1	**3.4 ± 1.4**	**3.0 ± 1.1**	0.4	**0.37**

Note. Length refers to profile length in kilometers. Bold values indicate those that meet the profile length reliability criteria presented in Table 4. rms = root-mean-square.

of the EM instrument of ±0.1 m over level ice (Haas et al., 2009). However, there was a presence of old FYI that formed in the Lincoln Sea polynya in fall 2008 with a mode of 2.2 m (Haas et al., 2010), which compared well with mean ground-based total thickness measurements of 2.1 m for FYI within the Lincoln Sea collected during May of 2010, 2011, and 2012 (Lange et al., 2015). Thus, we are confident in the accurate calibration of the EM instrument. Mean total thicknesses for the complete (e.g., level ice plus ridged ice) subprofiles (P1 to P4) ranged between 5.0 and 5.8 m with a combined-profiles mean of 5.3 m (Table 2). For measurements of level ice-only, mean total thicknesses ranged between 4.3 and 4.8 m with a combined mean of 4.5 m (Table 2). Modal total thicknesses for the complete subprofiles P1 to P4 ranged between 3.9 and 4.7 m with a combined mode of 3.9 m (Table 2 and Figures 4 and 5). For level ice only, modal total thicknesses were between 3.6 and 4.5 m with a combined-profiles mode of 3.7 m (Table 2). The largest difference between complete profile and level ice profile modal total thicknesses was observed for the northernmost subprofile P1 (Table 2 and Figure 4a), in agreement with the interpretation from the SAR data of that region being the most deformed. In contrast to subprofiles P1, P2, and P3, where the modal total thicknesses of the level ice were less than the modal total thicknesses of the complete subprofile, the modal total thickness of level ice in subprofile P4 was 0.2 m thicker than the modal total thickness of the complete subprofile. This was likely the result of the presence of thinner deformed sea ice (likely FYI) along P4, whose total thickness values overlapped with the mode of the level MYI, which is the dominant ice type along this subprofile (Table 2 and Figure 4d). These thinner deformed ice values were subsequently removed during level ice extraction, thus resulting in a thicker modal total thickness.

3.3.2. Summer Ice Thickness in Nares Strait

The full surveys (no filtering or floe extraction) had modal ice thicknesses between 2.0 and 2.7 m (Table 3). The ice thickness probability density functions for each of these five HEM surveys had a mode at 0.0 m corresponding to measurements over open water and confirming the accuracy of the instrument's calibration (Figure 6). It should be noted that the HEM thickness values in these summer surveys are equivalent to ice-only thickness, as no snow was present on the ice. A summary for each survey is provided in Table 3. Note that we did not compute mean ice thicknesses for the full surveys due to the presence of open water. The mean open water fraction for all summer surveys was 12% (individual survey range: 1–27%).

The HEM surveys include observations acquired over 12 separate, well-defined ice floes (Tables 1 and 2). Mean ice thicknesses for the complete floe profiles (including level and ridged ice) ranged between 2.8

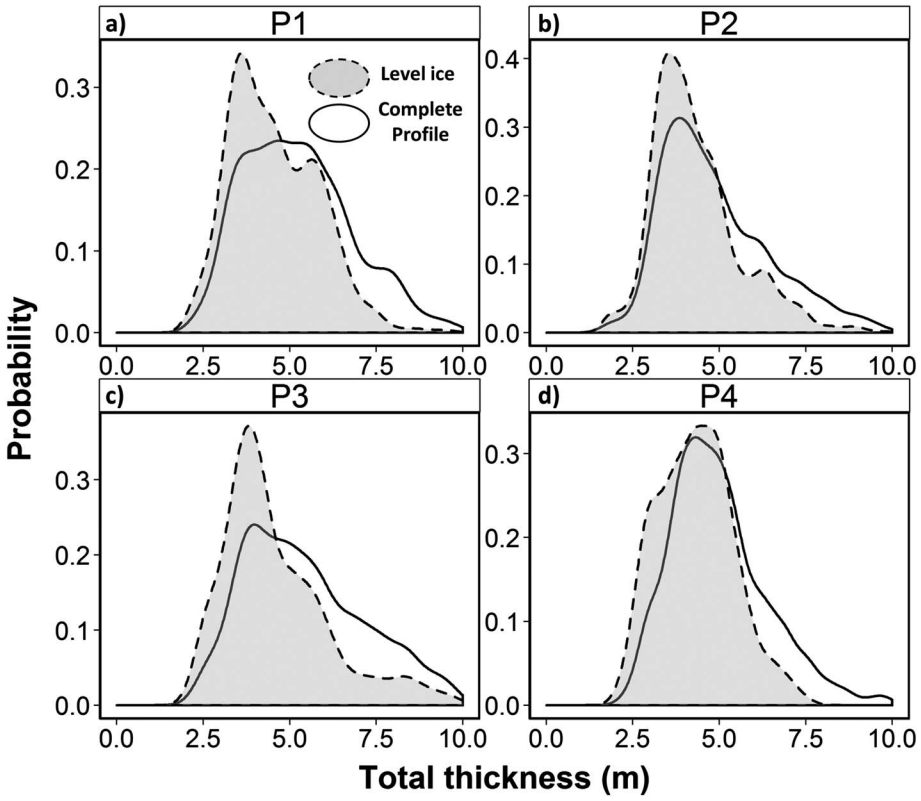

Figure 4. Total thickness distributions in spring showing the complete (ridged and level ice) and level ice-only components of the spring subprofiles: (a) P1, (b) P2, (c) P3, and (d) P4 (see map in Figure 1b).

and 4.5 m with a mean of 3.4 m for all floes (Table 2). Modal ice thicknesses for complete floe profiles ranged between 2.2 and 3.8 m with a combined mode of 2.5 m (Table 2). For the level ice profiles, modal ice thicknesses ranged between 2.1 and 3.0 m with a mode of 2.4 m for all profiles. Mean level ice thicknesses ranged between 2.6 and 3.6 m for individual floes, with a mean of 3.0 m for all floes (Table 2). Large differences (e.g., 0.7 to 1.2 m) between complete floe and level ice modal ice thicknesses were observed for floes F08, F09, and F11 (Table 2 and Figures 7h, 7i, and 7k). All remaining floes had small differences ($<$0.2 m) between the complete floe and level ice modal ice thicknesses (Table 2 and Figure 7). For all floes combined, the difference between complete floe profile and level ice modal ice thicknesses was only 0.1 m (Table 2); that is, there was little deformed ice.

3.4. Statistical Reliability of Airborne Survey Profile Lengths

Statistically reliable modal ice thicknesses could be obtained during summer with profile lengths of 15 km for level ice only and with profile lengths of 35 km for complete profiles (Table 4). A similar pattern was observed for summer mean ice thickness with representative profile lengths obtained at 5 km for level ice and 10 km for complete profiles (Table 4). Whereas in spring, we found that 10 km was a sufficient profile length to obtain reliable mean and modal total thicknesses (Table 4). Surface roughness (rms height) calculations showed no seasonal variability with minimum reliable profile lengths of 15 km for both spring and summer (Table 4). The full list of percent SE values for each profile length and subset is provided in supporting information Table S1.

3.5. Melt Rates

3.5.1. Melt Onset

Buoy observed melt onset dates were determined to be day of year 159 (9 June 2009) for the SVP buoy deployed at site 1, day of year 164 (14 June 2009) for the SVP buoy deployed at site 2 and day of year 161 (11 June 2009) for the Canister buoy (Figure 8a), that is, varying within only 5 days. ASCAT-derived melt onset occurred between days of year 160–164 (10–14 June 2009; Figures 8c–8g), in close agreement with the buoy

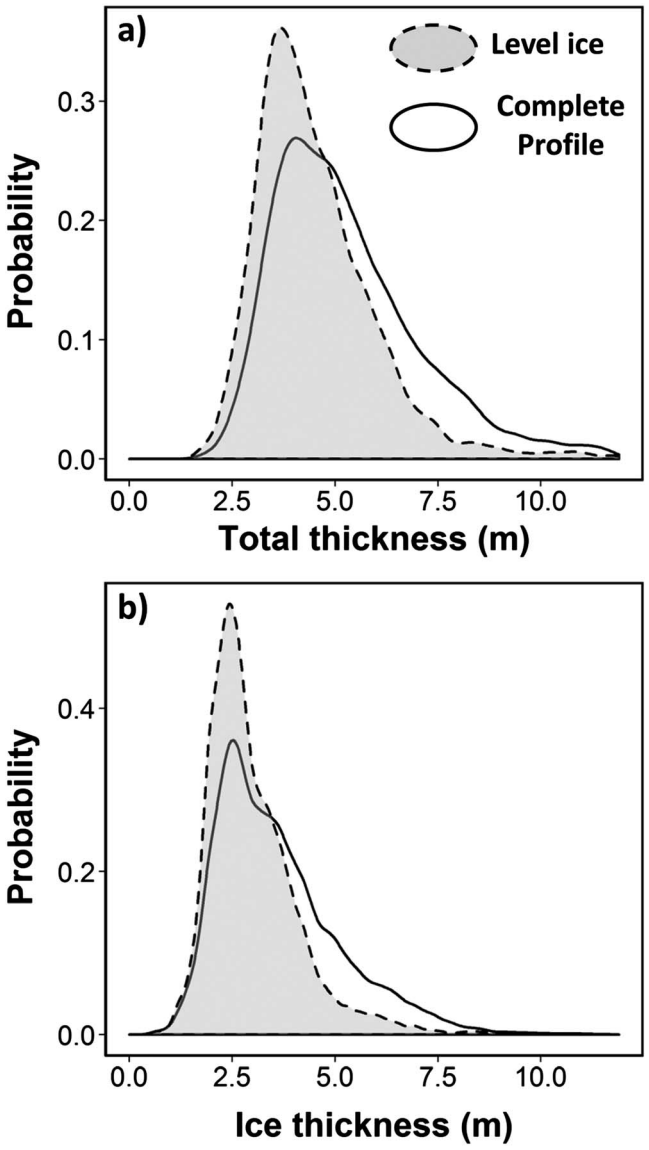

Figure 5. Thickness distributions showing the complete (ridged and level ice) and level ice-only components of (a) the combined April total thickness subprofiles P1 to P4 (Figure 4) and (b) the combined August floe ice thickness profiles (F01 to F12; Figure 7).

Table 3
Summary of the Full (No Filtering or Floe Extraction) Summer Surveys in Nares Strait

Survey	Modal ice thickness (m)	rms height (m)
16a	2.5	0.34
16b	2.5	0.35
18a	2.0	0.37
18b	2.6	0.43
19	2.7	0.37
All	2.4	0.37

data. Therefore, we use an average day of year 162 (12 June 2009) as the date of melt onset for the melt and energy budget analyses that follow.

The date when most of the snow had melted (i.e., the date when melt ponds, rather than wet snow, dominate the ice surface cover) was also derived from ASCAT backscatter time series and was determined to be day of year 200 (19 July 2009; supporting information Figure S3). Therefore, the duration of the snow melt period (melt onset to the onset of ponding: day of year 162 to 200) was 38 days and the duration of the melt season between the spring and summer thickness surveys (melt onset to survey dates: 162 to 230) was 68 days.

3.5.2. Melt Estimates

Total (ice plus snow) melt was estimated by subtracting the summertime modal ice thickness values from the springtime modal total thickness values. Total melt estimates derived from comparing the combined spring AEM subprofiles (P1–P4) to the combined summer HEM floe profiles was 1.4 m for the complete (level and ridged ice) and 1.3 m for level ice only (Table 5 and Figure 5). Subtracting the 0.42 m of snow resulted in a sea ice melt of 1.0 and 0.9 m for the complete and level ice-only profiles, respectively. Comparing subprofile P1 to floe F11 (the closest HEM floe profile and AEM subprofile pair, between ~3 and 20 km apart or ~10 km midpoint to midpoint) results in a total melt of ~1.3 m and sea ice melt of ~0.9 m for both the complete and level ice-only profiles (Table 5).

Using equation (1) and the range of sea ice melt between 0.9 and 1.0 m results in a seasonal net heat input for ice ($\boldsymbol{Q_i}$) with a range of 265 to 295 MJ/m^2 (Table 5). $\boldsymbol{Q_s}$ for 0.42 m of snow was 39 MJ/m^2 from 12 June to 19 July 2009. $\boldsymbol{Q_t}$ for snow plus ice ranged between 305 and 335 MJ/m^2. Applying these values to equation (2) using the melt duration period ($\boldsymbol{\Delta t}$) of 68 days for sea ice and 38 days for snow corresponds to seasonal net heat fluxes ($\boldsymbol{F_{net}}$) for sea ice plus snow in the range of 57 to 62 W/m^2 (Table 5). $\boldsymbol{F_{net,s}}$ for 0.42 m of snow was 12 W/m^2. Table 5 also includes uncertainty estimates discussed in section 4.5.

4. Discussion

4.1. Ice Thickness Variability and Representativeness of Results

The Lincoln Sea is home to the thickest sea ice in the Arctic Ocean and is expected to be home to the last remaining MYI as sea ice continues to decline and thin (Haas et al., 2010; Kwok et al., 2010; Laxon et al., 2013). However, there is large regional and interannual variability in total thickness within this region. Haas et al. (2006) observed modal total thicknesses for the Lincoln Sea of 3.9 m in May 2004, including a mean snow thickness of 0.3 m, and modal total thickness of 4.2 m including a mean snow thickness of 0.35 m during May of 2005. Haas et al. (2010) extended this Lincoln Sea total thickness time series and observed large interannual variability of springtime modal total thickness ranging between 3.2 and 4.4 m for the years 2004 to 2009. In 2009, Haas et al. (2010) observed large regional variability of modal total thickness in the Lincoln Sea, with modes from different surveys within the Lincoln Sea, ranging between 3.1 and 4.4 m. Here we used a subset of the AEM data presented in Haas et al. (2010), and the modal thicknesses for our profile of 3.9 m were within the range of observed total modal thicknesses for the region. However, the range of modal total thicknesses of the subprofiles was sensitive to the manner in which the spring AEM survey was partitioned into subprofiles of varying

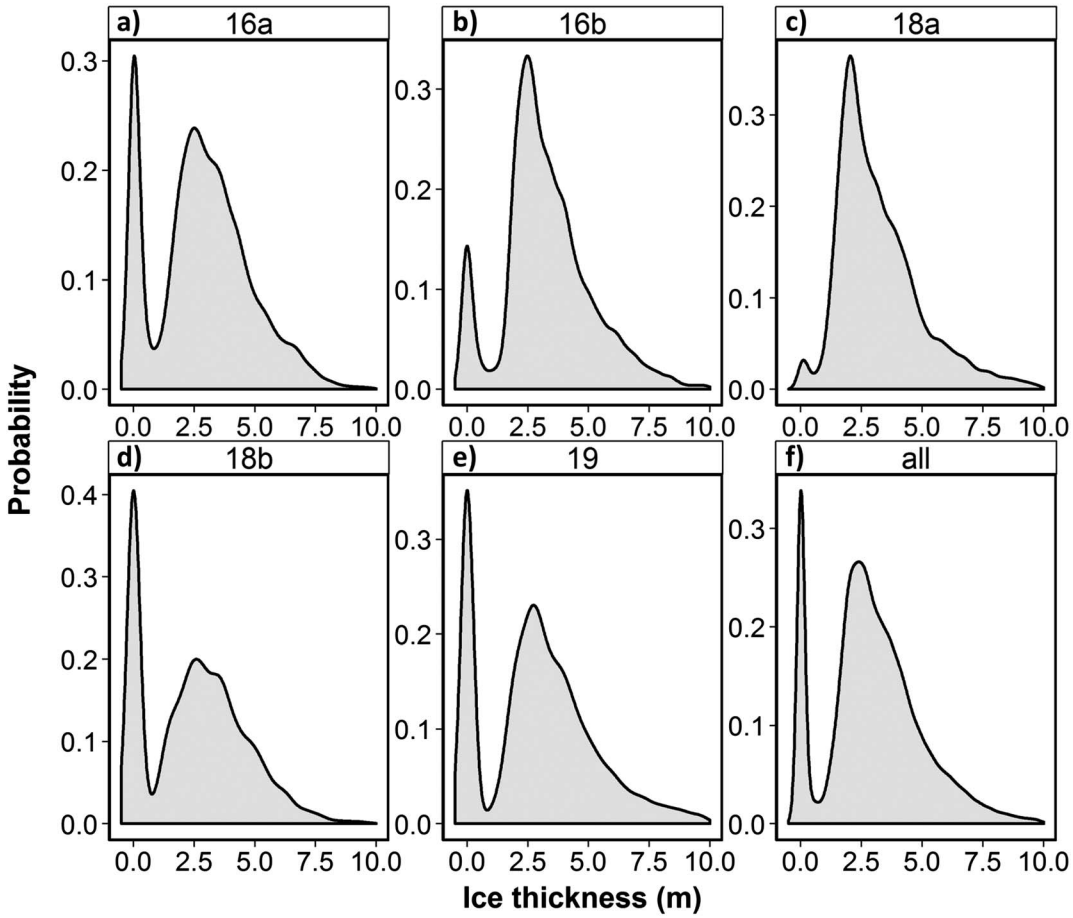

Figure 6. Ice thickness distributions from the full helicopter-borne electromagnetic surveys (no filtering or floe extraction) conducted during summer in Nares Strait on (a) 16 August 2017 profile "a"; (b) 16 August 2017 profile "b"; (c) 18 August 2017 profile "a"; (d) 18 August 2017 profile "b"; (e) 19 August 2017; and (f) all surveys combined.

locations and lengths. The high interannual and regional variability of ice thickness in this region highlights the potential for large uncertainties when trying to quantify the seasonal ice thickness cycle by comparing seasonal measurements that are sparse, both spatially and temporally. Nevertheless, the profile length reliability analysis provides a quantitative measure to identify valid/reliable comparisons (i.e., comparing profiles that meet the reliability criteria; see section 4.4).

4.2. Comparison With Other Summer Thickness and Draft Observations in Nares Strait

Ryan and Münchow (2017) present an extensive ice draft time series for Nares Strait (~80.5°N) between 2003 and 2012 using moored upward looking sonar (ULS) arrays. Unfortunately, no observations were made during August of 2009; however, Ryan and Münchow (2017) observed daily median ice draft values in the range of 2 to 3 m (~2.2- to 3.3-m ice thickness equivalent at bulk ice density of 900 kg/m^3) for the month of July 2009. This is comparable to our modal ice thickness observations of level ice between 2.1 and 3.0 m (median: 2.5 to 3.0 m). Furthermore, Ryan and Münchow (2017) showed that over the entire time series median ice draft was 0.8 m with annual median draft values ranging from 0.5 to 1.5 m (~0.9 m, range: 0.6 to 1.7-m ice thickness equivalent). These overall time series values are slightly thinner than our observed summer modal thicknesses, which is likely the result of larger amounts of FYI and brash/rubbled ice between larger floes within the drifting ice profiled by the ULS. Ryan and Münchow (2017) showed that 38% of the ice consisted of MYI and thicker sea ice drafts around 2 m contributed proportionately the most in terms of ice volume.

We are aware of only one other HEM campaign conducted in Nares Strait during summer. HEM surveys were carried out by Prinsenberg (2014) during summer 2013 (21–24 August), in the same study region as ours.

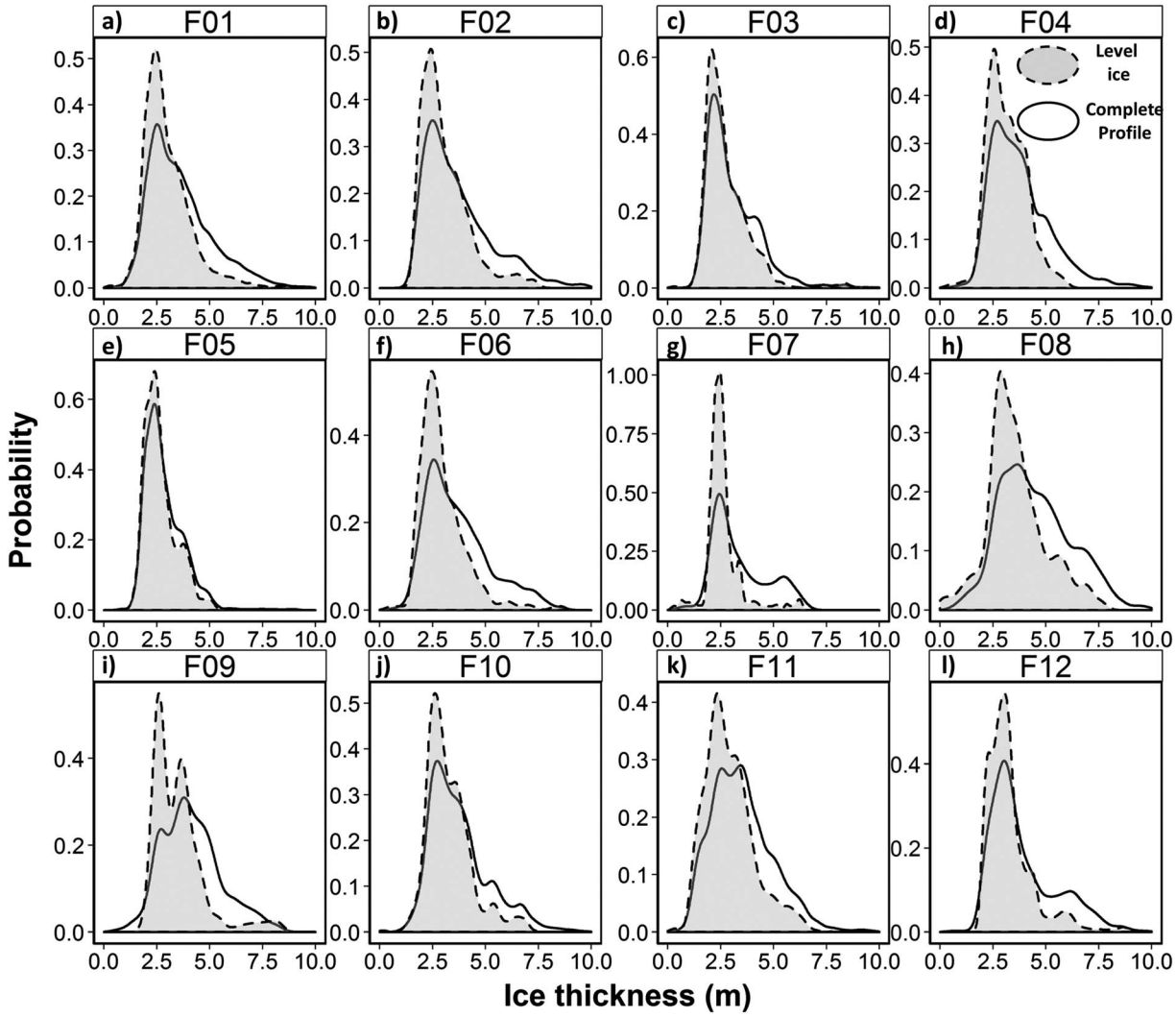

Figure 7. Ice thickness distributions showing the complete (ridged and level ice; solid lines) and level ice-only (dashed lines, shaded) components of the helicopter-borne electromagnetic surveys for (a–l) floes F01 to F12, respectively.

Table 4
Summary of the Minimum Reliable Profile Lengths (km) Compared for Spring and Summer, Between Modal Thickness, Mean Thickness, and Surface Roughness (rms) and Between Complete (Level Plus Deformed Ice) and Level Ice Only

Statistical summary	Profile subset	Minimum reliable profile length (km)	
		Spring	Summer
Modal thickness	Complete profile (level + deformed ice)	10	35
	Level ice only	10	15
Mean thickness	Complete profile (level + deformed ice)	10	10
	Level ice only	10	5
rms height	Complete profile (level + deformed ice)	15	15

They were conducted with a different HEM system that was fixed mounted to a helicopter and is described in Prinsenberg et al. (2002). Based on seven across-strait transects, ranging in length (excluding open water regions) from 22 to 116 km, modal thicknesses ranged between 1.6 and 2.0 m and mean thicknesses between 1.8 and 2.2 m, with an overall mode of 1.8 m and mean of 1.9 m. These are 0.6 to 2.3 m thinner than our range of floe modal and mean thicknesses of 2.2–3.8 and 2.8–4.5 m, respectively, in 2009. Overall, in summer we found ice floe modal thicknesses of 2.5 m and mean of 3.4 m (Table 2), which are 0.7 and 1.5 m thicker than in 2013, respectively. The difference in both mean and modal ice thicknesses between summers of 2009 and 2013 could also be due to differences in the ice conditions between these study years. Comparing National Snow and Ice Data Center sea ice age data (Tschudi et al., 2016) from spring 2009 with spring 2013 within the Lincoln Sea shows that there was a larger fraction of FYI and younger MYI in 2013 compared to 2009 (Figures 9c and 9d). This also suggests that the ice was already thinner in spring 2013 compared to 2009, which

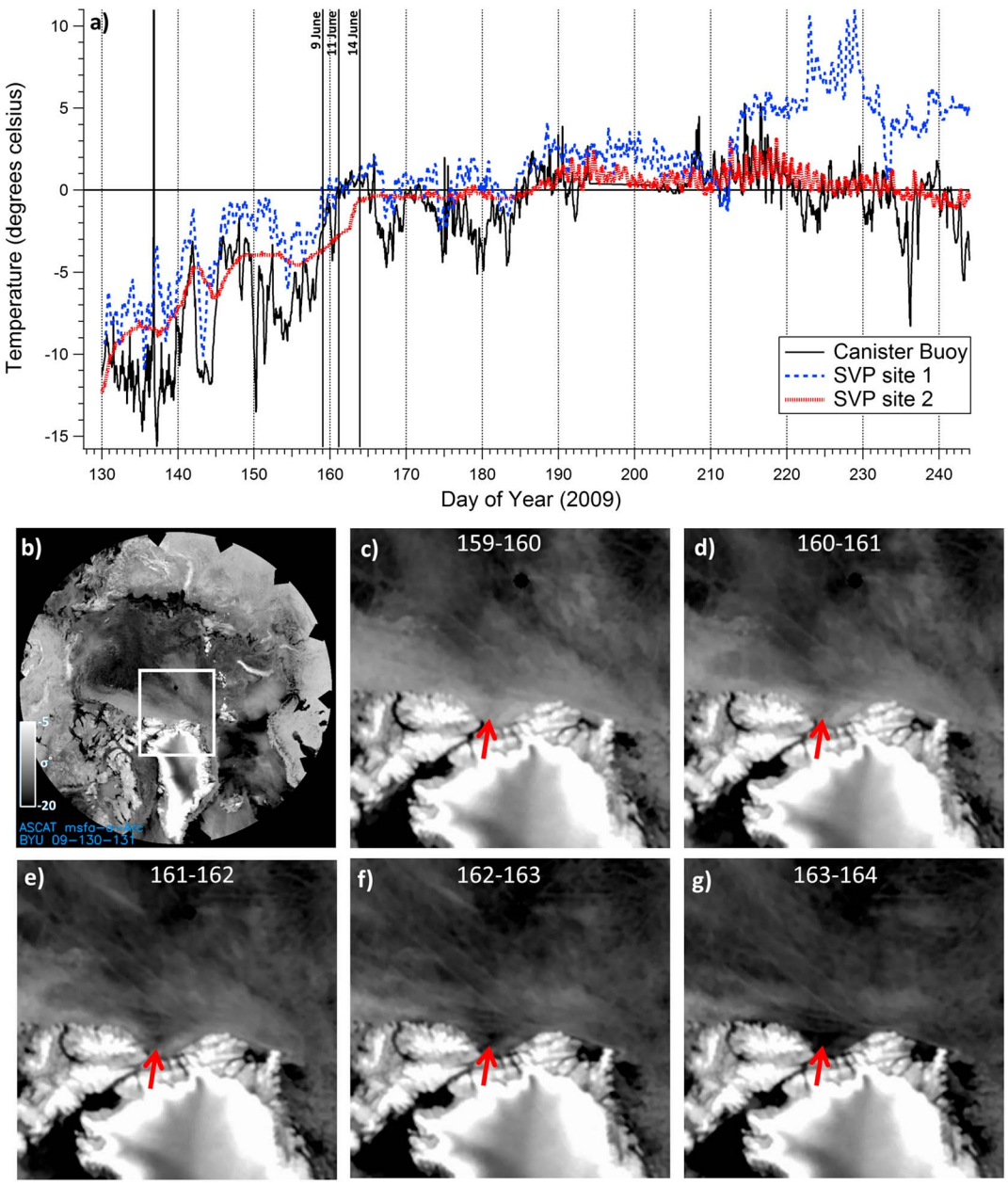

Figure 8. (a) Surface temperature time series from 2 SVP and 1 Canister buoys deployed in May 2009. (b) Overview Advanced Scatterometer backscatter map of days of year 130–131 (11–12 May 2009) with inset showing coverage for (c) to (g). Grayscale bar represents backscatter intensity (σ°).(c–g) Two-day composite Advanced Scatterometer backscatter maps, showing the onset of melt during 2009, for (c) days 159–160 (9–10 June); (d) days 160–161 (10–11 June); (e) days 161–162 (11–12 June); (f) days 162–163 (12–13 June); and (g) 163–164 (13–14 June). Red arrows show region of interest. Data were obtained from the National Aeronautics and Space Administration sponsored Scatterometer Climate Record Pathfinder at Brigham Young University through the courtesy of David G. Long.

may explain the thinner summer ice thicknesses in 2013 observed by Prinsenberg (2014) compared to our study.

The Prinsenberg (2014) data, summarized by floe size, showed only three surveyed floes that were wider than 2 km. In contrast, all the floes considered in our 2009 survey were wider than 2 km. One 2013 floe had a width of 4.2 km and a mean thickness of 2.5 m (Prinsenberg, 2014), which is ~1 m thinner than our smallest floes of comparable width (floes F01 and F07), which had mean thicknesses of 3.6 and 3.4 m, respectively (Table 1). In 2013, over half of the 140 identified floes larger than 100 m had mean ice thicknesses between 2.5 and 3.5 m. Only 3 of our 12 floes surveyed in 2009 had mean thicknesses between 2.5 and 3.5 m, with the remaining 9

Table 5
Melt and Heat Flux Estimates Based on Different Survey and Profile Comparisons

Survey	Season	Complete	Level ice
All AEM subprofiles (P1 to P4) modal total thicknesses (m)	Spring	3.9	3.7
All HEM floe profiles modal ice thicknesses (m)	Summer	2.5	2.4
	Modal snow depth	0.42 ± 0.09	0.42 ± 0.09
	Total melt (m)	1.4 ± 0.1	1.3 ± 0.1
	Sea ice melt (m)	1.0 ± 0.2	0.9 ± 0.2
	Melt rate (cm/day)	1.5 ± 0.3	1.2 ± 0.3
	Q_i (MJ/m^2)	295 ± 60	265 ± 60
	$F_{net,i}$ (W/m^2)	50 ± 10	45 ± 10
	Q_t (MJ/m^2)	335 ± 69	305 ± 69
	[a]F_{net} (W/m^2)	62 ± 13	57 ± 13
P1 modal total thicknesses (m)	Spring	4.7	3.6
F11 modal ice thicknesses (m)	Summer	3.5	2.3
	Modal snow depth	0.42 ± 0.09	0.42 ± 0.09
	Total melt (m)	1.3 ± 0.1	1.3 ± 0.1
	Sea ice melt (m)	0.9 ± 0.2	0.9 ± 0.2
	Melt rate (cm/day)	1.3 ± 0.3	1.3 ± 0.3
	Q_i (MJ/m^2)	265 ± 60	265 ± 60
	$F_{net,i}$ (W/m^2)	45 ± 10	45 ± 10
	Q_t (MJ/m^2)	305 ± 69	305 ± 69
	[a]F_{net} (W/m^2)	57 ± 13	57 ± 13

Note. AEM = airborne electromagnetic; HEM = helicopter-borne electromagnetic.
[a]F_{net} was calculated for snow plus ice by taking the sum of $F_{net,i}$ and $F_{net,s}$ 12 ± 3 W/m^2.

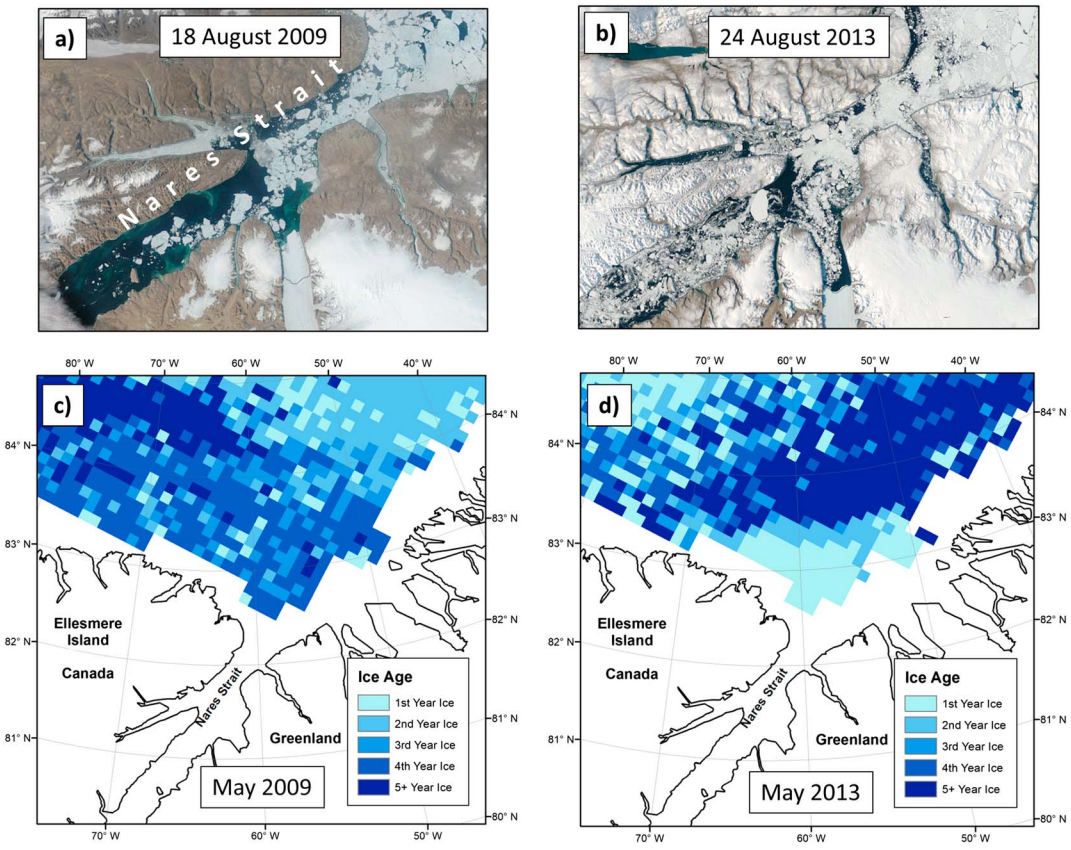

Figure 9. Moderate Resolution Imaging Spectroradiometer images of northern Nares Strait acquired on (a) 18 August 2009 and (b) 24 August 2013. Sea ice age maps of the Lincoln Sea for week 18 (beginning of May) of (c) 2009 and (d) 2013. Sea ice age data acquired from National Snow and Ice Data Center (Tschudi et al., 2016).

floes having mean ice thicknesses >3.5 m. The fact that the majority of surveyed floes had widths smaller than 500 m together with the difference in spring ice age composition in the Lincoln Sea suggests that the floes surveyed in 2013 were thinner during spring than the larger sized floes surveyed in 2009. This would have caused the thinner 2013 floes to be more susceptible to break up into smaller floes during their transit southward into and through Nares Strait (e.g., Hwang et al., 2017). Another possible explanation for the large thickness differences could be that when the sea ice was in the Lincoln Sea in 2013 (before melt), it may have been more heavily deformed during spring given that 2013 had anomalously strong convergent ice drift compared to weak convergence in 2009 (Kwok, 2015). The strong convergence together with presumably thinner and younger ice coverage during spring 2013 would have resulted in the sea ice fracturing into smaller floes, which could have led to the observed smaller floes in summer 2013, and creating larger ridge/rubble fields prior to melt onset 2013. Although convergence of sea ice results in an overall increase in thickness due to deformation, the unconsolidated structure of deformed ice would have resulted in larger regions of brash, rubble fields during summer breakup. We speculate that the brash and rubbled sea ice fields would have been more susceptible to melt due to increased surface area and water entrainment within the sea ice rubble fields enhancing absorption of solar radiation and increased mobility allowing for mechanical degradation of the rubble fields.

To understand the differences between summer ice thickness in Nares Strait in 2009 and 2013, we qualitatively analyzed differences in ice arch break up and ice conditions in both years using a time series of MODIS images (not presented here, available online at https://worldview.earthdata.nasa.gov). Different ice arch regimes developed within Nares Strait in 2009 and 2013. These two arch regimes were previously identified by Kwok et al. (2010) and Ryan and Münchow (2017). In 2009 the ice arch formed at the northern extent of Nares Strait (82.4°N) and broke up on 6 July 2009. In contrast, in 2013 the ice arch formed farther south (79.2°N) and ice breakup occurred in stages: On 12 July 2013 the ice arch began to disintegrate and retreated up to 81.3°N where another arch formed and remained stable until 20 July 2013 when it failed and sea ice began to freely drift southward from the Lincoln Sea. Ryan and Münchow (2017) showed ice draft within Nares Strait had annual median drafts that were thicker in years when the southern ice arch formed (e.g., 2013) in comparison to when the northern ice arch formed (e.g., 2009). Based on this premise, we would have expected to observe thicker ice in 2013 compared to 2009; thus, the ice arch regimes do not explain the thicker summer sea ice in 2009.

Furthermore, there was an obvious contrast in sea ice concentration and floe sizes in both Nares Strait and the Lincoln Sea between 2009 and 2013(Figure 9). Large ice floes dominated the ice field in Nares Strait and the southern Lincoln Sea in the 2009 MODIS image (Figure 9a). In contrast, the 2013 MODIS image (Figure 9b) shows only a few large floes with a dominance of small floes interspersed by substantially large areas of brash/rubbled ice (e.g., darker white appearance of sea ice between floes). The dominance of smaller floes and brash/rubbled ice fields could have enhanced the oceanic, surface layer heat flux, and increased melt in comparison to summer 2009.

This discussion shows that it is difficult to compare observations from different years in a highly mobile, melting ice region. However, it should also be noted that differences between the used EM instruments could also have contributed to the observed difference between the mean thicknesses in both years due to the different characteristics of the used EM instruments. The fixed-mounted system of Prinsenberg et al. (2002) has a smaller coil spacing (1.2 m) than our EM Bird (2.67 m). This reduces the EM penetration depth and the sensitivity to thicker, deformed ice of the fixed-mounted system, making it less sensitive to the thickness of pressure ridges. This would affect the retrieved mean thickness more than the retrieved modal thickness of level ice whose accuracy depends more on the instrument's signal-to-noise ratio.

4.3. Sea Ice Floe Tracking, Drift, and Volume Flux Estimates

Computer algorithms for tracking sea ice using SAR imagery have difficulties tracking individual floes over long distances and differentiating sea ice from water during summer (e.g., Komarov & Barber, 2014; Kwok, 2005, 2010; Kwok et al., 2010). Therefore, we applied a manual tracking system to ensure accurate individual floe delineation and tracking. Computerized sea ice tracking systems, which require minimal human interaction (e.g., Kwok, 2005; Kwok et al., 2010), however, are ideal for estimating ice area and volume fluxes. Annual ice area fluxes through Nares Strait during the period 1997 to 2002 were on average 33×10^3 km^2 (Kwok, 2005) and increased to 42×10^3 km^2 during the extended period 1997 to 2009 (Kwok et al., 2010).

The extended period includes two years, 2007 and 2008, with anomalously high ice export due to the absence or delayed formation of an ice arch in Nares Strait (Kwok et al., 2010). During our 2009 study year, the ice arch formed on 16 January, which is in agreement with the average date of arch formation of 12 January (Kwok et al., 2010). Therefore, we used the average annual area flux of 33×10^3 km^2 in combination with our total thickness measurements to estimate the ice volume flux for the annual cycle 2009 to 2010.

As there were no satellite-based (ICESat or CryoSat) ice thickness observations in 2009, we provide an essential seasonal ice thickness data set to fill an important temporal gap in ice flux estimates through Nares Strait. Taking the average of our spring ice-only mean of 4.9 m (i.e., 5.3-m total thickness minus 0.42 m of snow) and summer mean of 3.4 m (Table 2) results in an annual mean ice thickness of 4.2 m. Using this value of 4.2 m, we calculated an estimated annual (2009–2010) ice volume flux of 139 km^3 through Nares Strait. This is in good agreement with the 5-year average volume flux of 141 km^3 (range 33 to 254 km^3) found by Kwok et al. (2010). Kwok et al. (2010) used annual average (fall and winter) sea ice thickness estimates between 4.3 and 5.5 m, an observational update from the assumed 4 m used by Kwok (2005). The range in ice thickness values used for the flux estimates has a large influence on the overall annual volume flux estimates. Furthermore, we demonstrated that the representativeness of the modal or mean total/ice thickness measurements used depends on profile length. Therefore, improvements in spatiotemporal coverage and resolution of the thickness observations are desirable. For example, using our mean summer ice thickness value of 3.4 m results in an annual volume flux of 112 km^3, whereas using the mean spring thickness value of 4.9 m results in an annual volume flux estimate of 162 km^3. Furthermore, the sea ice in the Lincoln Sea only became mobile later in the summer, when it was already melting; therefore, the inclusion of spring thickness observations in our mean annual ice thickness estimate may lead to the overestimation of annual ice volume flux.

4.4. Importance of Individual Floe Tracking and Level Ice Extraction

Although large differences between level ice profile and complete profile modal thicknesses were only observed for 3 of 12 summer HEM floe surveys and 1 of 4 spring AEM subprofiles (Table 2), it still emphasizes the importance of extracting level ice regions from airborne surveys in order to characterize different sea ice regimes. These results do show the potential for thinner deformed ice portions of the thickness profile to overlap the thermodynamically grown level ice component of the thickness distribution and produce a false interpretation of the level ice modal thickness (Figures 4 and 7). Furthermore, we observed no change in the minimum profile length required for representative spring mean and modal total thickness when comparing the level ice profiles with the complete profiles (Table 4). Whereas in summer, level ice extraction resulted in half the required profile length for representative ice thickness surveys. These results suggest that in summer level ice extraction is more important in terms of improving (i.e., decreasing) the required profile length for representative sea ice thickness surveys.

Three backtracked floes (F08, F09, and F11) were found to originate within the more heavily deformed ice region of the spring surveys. These floes had the largest difference between level ice only and complete profile modes. Subprofile P1 from the spring AEM survey in April, which was conducted in closest proximity to these three floes (F08, F09, and F11), also showed the largest difference between level ice only and complete profile modes, indicating a higher fraction of deformed ice in the floe profiles within the high backscatter region. Kwok (2015) also observed a gradient of increased deformation from east to west toward the coast of Greenland within the Lincoln Sea. This is consistent with our interpretation that the difference in backscatter in the east and west Lincoln Sea is a result of differences in the surface roughness and amount of deformed ice in these regions. The close proximity of floe F11's backtracked location to subprofile P1 combined with the east to west surface roughness and deformed ice gradient indicate that floe F11 and subprofile P1 are from a similar sea ice regime.

Based on our conclusion that floe F11 and subprofile P1 were representative of sea ice from the same region, it makes sense that comparing their thickness distributions in spring and summer should provide the most reliable estimates of the seasonal ice thickness cycle. This seasonal thickness difference was determined to be 1.3 m, both for modal and mean thickness (Table 4). These findings strengthened our conclusion that floe F11 and subprofile P1 were representative of sea ice from the same localized region. Thus, this comparison provides the best estimate of total melt between the spring and summer thickness surveys without the need to remove the influence of the deformed ice component from the thickness distribution.

When comparing the full data set surveys, there was slightly more variability in the estimated seasonal thinning of 1.3 m for level ice only and 1.4 m for the complete profiles (Table 4); however, this is still within the ±0.1-m accuracy of the EM instrument. Our profile length reliability analysis indicated that when comparing seasonal thickness distributions of sea ice originating from a similar region, spring surveys of 10 km and summer surveys of 35 km can provide representative estimates of the seasonal ice thickness cycle for the Lincoln Sea. Using these profile lengths are a useful guideline if high accuracy floe tracking is not possible. Seasonal thickness change estimates, without the use of floe tracking methods, however, may still produce larger uncertainty based on the large range of modal thicknesses observed due to large interannual variability or depending on if level ice extractions are conducted. We must note that in other regions of the Arctic Ocean minimum representative profile lengths will vary and depend on ice drift patterns, mixture of ice types, and amount of deformation. For example, Rabenstein et al. (2010) showed that representative profile lengths for sea ice around the North Pole ranged between 15 and 50 km, whereas they could be up to 100 km for more deformed sea ice northeast of Greenland. Furthermore, Beckers et al. (2015) also noted increases in representative survey lengths with increases in divergence and for ice originating from different regions and regimes.

Seasonal comparisons of all possible combinations of the shorter subprofiles with the individual floe surveys (~10 km), with modal thicknesses ranging from ~3.9 to 4.7 m in spring and ~2.2 to 3.8 m in summer, resulted in a range of seasonal thickness differences of 0.1 to 2.5 m. When comparing the level ice-only surveys, the range of seasonal thickness differences was between 0.5 and 2.4 m. By comparing modal thicknesses between spring and summer, which only meet the reliability requirements (P1–P4, spring all, F01, F11, summer all; Table 2), the range is only slightly better between 0.4 and 2.2 m. We note that level ice extraction can substantially reduce profile length and for some of the presented profile subsets (Table 2) the extracted level ice regions were below the reliability requirements. Level ice subprofile P1 had a modal thickness of 3.6 m but a length of only 6 km, which was below the reliability criteria. Nevertheless, by combining subprofiles P1 and P2 we achieve a reliable profile length of 10 km and still maintain a modal thickness of 3.6 m. When comparing modal thicknesses for level ice-only (sub) profiles, which meet the profile length requirements (P1 + P2, spring all, F01, F11, summer all; Table 2) the seasonal thickness difference uncertainty is substantially reduced to 1.1 to 1.4 m. These results suggest that it is important to really compare the same ice and therefore that floe tracking is a crucial aspect of making seasonal ice thickness cycle estimates. We have also indicated that level ice extraction and reliability analysis are important in terms of reducing uncertainty in the level ice seasonal thickness change estimates. Furthermore, we showed that level ice extraction is important for characterizing sea ice regimes (e.g., regions of heavily deformed ice and/or with high ridge densities), potentially minimizing the profile lengths required to obtain representative thickness estimates and to ensure accurate representation of the level ice component of the thickness distribution.

4.5. Uncertainty and Comparison of Melt Estimates

Possible sources of uncertainties within our melt estimates can be due to the accuracy of the instrument (±0.1 m), regional and interannual variability of snow thickness observations, and variability of the snow and ice cover between the spring observations and time of melt onset. The most extensive in situ snow thickness data set for the Lincoln Sea showed mean values of 0.39 ± 0.06 m during spring 2017 (Haas et al., 2017) with an almost exact agreement to a well-used snow climatology value of 0.38 m (Warren et al., 1999) and in good agreement to our 0.42 m. The Warren snow climatology (Warren et al., 1999) is one of the most widely used snow data sets in the Arctic; thus, we use their reported rms error of 0.09 m for the uncertainty in our snow depth measurements. Furthermore, based on a time series spanning 1957–2014 Howell et al. (2016) reported $<$0.05 m of snow accumulation and ~0.15 m of landfast FYI growth near Alert, Ellesmere Island, during the period April to June, that is, the period between our spring survey and the onset of melt. The snow accumulation during that time is less than the reported rms error of 0.09 m. The ~0.15 m of ice growth for FYI during this period likely means that sea ice thicker than 3 m would have substantially less ice growth, if any at all. We assumed negligible ice growth during the period April to June for the surveyed MYI ($>$3 m). Thus, we used margins of error of ±0.09 m for snow depth estimates, of ±0.1 m for ice and total thickness estimates, and we used a combined error margin of ±0.2 m for ice melt estimates.

Our estimated total melt was 1.3 ± 0.1 m. This includes an assumed snow depth of 0.42 m (±0.09) in spring (the modal snow depth of nearby in situ measurements), resulting in a total ice melt of 0.9 ± 0.2 m. This

translates to a seasonal net heat input of 305 ± 69 MJ/m^2 (262 ± 60 MJ/m^2 for ice only) and seasonal net heat flux of 57 ± 13 W/m^2 (45 ± 10 W/m^2 for ice only). The amount of solar radiation absorbed by the snow, ice, and ocean surfaces within the central Arctic during summer (June to August) is approximately 65 W/m^2 (Ohmura, 2012), which is sufficient to account for the heat flux of 57 W/m^2 required to melt the estimated 0.9 m of ice and 0.4 of snow. Within the Lincoln Sea, however, the amount of solar radiation absorbed by the snow, ice, and ocean is likely less than the 65 W/m^2 reported for the central Arctic Ocean. This is due to the denser ice cover and thicker snow and ice pack in this region, which would reflect more solar radiation back to the atmosphere compared to the central Arctic. It is likely that solar radiation fluxes alone cannot explain the total amount of snow and ice melt we observed; thus, oceanic and atmospheric heat fluxes likely had an important contribution. Due to a lack of oceanic and atmospheric observations within the Arctic, in general, it is difficult and beyond the scope of this study to disentangle the different components of the energy budget.

Our 0.9 ± 0.2 m of ice melt is comparable to sea ice melt of 0.88 m observed by Untersteiner (1961), which was conducted between 82°N and 84°N (similar available solar energy) and total thicknesses of ~3.4 m. The Untersteiner (1961) study was conducted in 1957–1958, during a colder Arctic climate and an overall older, thicker, and more extensive ice pack (Maslanik et al., 2011). Perovich and Richter-Menge (2015) presented a more recent account of sea ice melt observations based on IMB data, which demonstrated large regional and temporal variability in total melt (0.16 to 2.94 m). Their database included 11 IMBs deployed within the PIZ (referred to as intermediate region in Perovich & Richter-Menge, 2015). Only five of these IMBs had comparable thicknesses (>2.5 m) to our study. The total melt for these five IMBs ranged between 0.4 and 1.26 m, including between 0.05 and 0.22 m of snow. The most representative comparison is one IMB that was deployed within the Lincoln Sea during spring 2013 with an initial total thickness of 3.57 m and a total melt of 1.12 m (including 0.08 m of snow), which is comparable but slightly smaller than our total melt of 1.3 ± 0.1 m. This 2013 IMB was deployed on a MYI hummock and therefore likely was not located in a melt pond during the following melt season. Not accounting for the melt of ponded ice will underestimate the magnitude of total melt due to the increased solar absorption and surface melt at the locations of melt ponds (Nicolaus et al., 2012; Perovich et al., 2003). Assuming the 2013 IMB is representative of unponded regions and that our estimates include ponded ice melt we can then differentiate the contribution of ponded versus nonponded melt using our total melt estimate of 1.3 m. Using a range of melt pond coverage for MYI between 15% and 24% (Nicolaus et al., 2012; Perovich et al., 2003; Rabenstein et al., 2010) results in a total melt rate for ponded ice between 1.5 and 2.4 m. This range is highly sensitive to variations in the pond coverage estimates. Nevertheless, it is consistent with the possible ~1.9 m of total melt for ponded ice considering ice surface melt of up to ~1 m (Hanson, 1965; Untersteiner, 1961) and bottom ice melt of up to 0.92 m within the PIZ (Perovich & Richter-Menge, 2015). These results emphasize the potential for large floe-scale variability in melt rates that may not be captured by single IMB observations, particularly if these observations are only from hummock ice and do not include melt ponds or vice versa.

Differential melt on the same floe is also apparent from sea ice surface topography profiles of typical spring MYI, which showed variations in surface topography of 1 m over level ice surveys on the same MYI floe (Lange et al., 2017). If we attribute the variability of sea ice surface topography on a level MYI floe to thermodynamic melting processes, then the difference in elevation from the maximum to minimum points would be the cumulative differential surface melt over the number of experienced summer melt periods. Assuming an ice age of 4 years (i.e., three summer melt periods) for a MYI floe with a mean thickness of ~3.5 m and 1-m elevation difference between minimum and maximum surface height translates to an average melt rate differential of 0.33 m/year between hummocked and melt ponded regions of the same floe. This only considers surface melt so the annual variability of differential melt rates on the same ice floe is likely larger than 0.33 m if bottom ice melt is also included. Again, this highlights the variability of melt processes on floe scales and exemplifies the importance of the floe-scale ice thinning estimates presented here.

5. Conclusions

In this study we presented a Lagrangian approach to quantify summer sea ice melt in which MYI floes that were surveyed within Nares Strait during summer were backtracked, using satellite imagery, to a region in close proximity (~5 km) to spring ice thickness surveys carried out in the Lincoln Sea. This approach

reduced the influence of regional sea ice thickness variability on the spring to summer comparison and provided greater confidence in the accuracy of the derived summer thinning and melt estimates. Our estimated total (snow plus ice) summer melt was 1.3 ± 0.1 m (0.4 ± 0.09 m of snow melt and 0.9 ± 0.2 m of ice melt). This translates to a seasonal net heat input of 305 ± 69 MJ/m^2 (262 ± 60 MJ/m^2 for ice only) and seasonal net heat flux of 57 ± 13 W/m^2 (45 ± 10 W/m^2 for ice only), which is unlikely to be explained by solar radiation fluxes alone. Furthermore, our approach provides an improvement on traditional IMB estimates because it integrates the melt over larger spatial scales, where melt can be highly variable due to differential melt experienced between melt ponds, bare ice, hummocks, and ridges.

Major uncertainties arose from the fact that we were not able to resurvey exactly the same ice but only similar ice fields, which resulted from insufficient advance planning of the summer surveys as no real-time SAR images were available to us at the time. Furthermore, we were not able to influence the cruise timing and trajectory in order to revisit some of the ice marked by buoys. Future summer AEM surveys should therefore be better coordinated with spring surveys, and real-time ice tracking should be attempted with buoys deployed in spring and with a continuous record of SAR images following the surveyed ice from spring to summer. Such real-time data are available nowadays, for example, through the Alfred Wegener Institute's FramSat and IceGIS systems on board the German research icebreaker Polarstern. With these better planning tools we plan to carry out another comparison of spring and summer ice thicknesses in the Lincoln Sea and Nares Strait by continuing AEM surveys and buoy deployments in spring within Alfred Wegener Institute's annual IceBird program and by performing HEM surveys over the same ice during the Swiss Greenland Circumnavigation Expedition (https://polar.epfl.ch) in August 2019.

Compared to ULS measurements, which provide only local ice draft measurements but for a long time, AEM surveys can provide regional information with controlled spatial coverage. However, using manned aircraft they cannot be maintained over longer time periods and therefore only represent temporal snapshots. Nares Strait would be ideal for monitoring ice thickness with a combination of ULS and AEM, where the ULS observe temporal changes along the main northeast to southwest drift direction, while AEM surveys across the strait could provide information about the potential across-drift ice thickness variability.

Our discussion of the energy balance uncertainties based on the observed ice melt and the contributions of individual energy balance components shows the importance of carrying out interdisciplinary observation campaigns that include boundary layer meteorologists, sea ice geophysicists, and oceanographers to accurately observe the energy fluxes in the air, ice, and water and to relate them to the observed ice thickness changes. Toward that goal we will carry out the Multidisciplinary drifting Observatory for the Study of Arctic Climate (https://www.mosaic-expedition.org) project in the winter and summer of 2020 where the fate of numerous ice floes in the Transpolar Drift will be observed throughout a complete seasonal cycle and when the dynamic and thermodynamic changes of the ice thickness distribution will be observed in combination with atmospheric and oceanic boundary conditions.

Acknowledgments
This project would not have been possible without the collaboration with the members of the 2009 CATs cruise and the invitation by the cruise leader Humfrey Melling. The crew of the *CCGS Henry Larsen* were very helpful with preparation of HEM flights and logistics of the cruise. The CATs cruise would not have been possible without support from the International Polar Year (IPY 2006-SR1-CC-135). We would like to thank Monica Doorenbos for her help processing MODIS imagery. MODIS and ENVISAT satellite images were graciously provided, free of charge, by the National Aeronautics and Space Administration (NASA) and the European Space Agency (ESA), respectively. ENVISAT imagery is copyrighted by ESA, the images used here were acquired through ESA projects EO500: Formation, transport, and distribution of sediment-laden sea ice in the Arctic Shelf seas; and EO1241: Validation of CryoSat sea ice retrievals. ASCAT data were obtained from the NASA sponsored Scatterometer Climate Record Pathfinder at Brigham Young University through the courtesy of David G. Long. Funding for this project was largely provided by Alberta Innovates-Technology Futures, the Alfred Wegener Institute for Polar and Marine Research, the Canadian Federal Programme on Energy Research and Development, the Nunavut Department of Economic Development and Transportation, Petro-Canada Ltd., the Canadian Circumpolar Institute (CCI), Indian and Northern Affairs, the Natural Sciences and Engineering Research Council of Canada (NSERC), and the Northern Scientific Training Program (NSTP) through the Department of Indian Affairs and Northern Development. Compute Canada provided resources for storing and processing the satellite imagery and laser data. All data are available from the PANGAEA database https://doi.org/10.1594/PANGAEA.778685 and https://doi.pangaea.de/10.1594/PANGAEA.895115.

References

Barber, D. G., Babb, D. G., Ehn, J. K., Chan, W., Matthes, L., Dalman, L. A., et al. (2018). Increasing mobility of high Arctic sea ice increases marine hazards off the east coast of Newfoundland. *Geophysical Research Letters*, *45*(5), 2370–2379. https://doi.org/10.1002/2017GL076587

Beckers, J. F., Renner, A. H. H., Spreen, G., Gerland, S., & Haas, C. (2015). Sea-ice surface roughness estimates from airborne laser scanner and laser altimeter observations in Fram Strait and north of Svalbard. *Annals of Glaciology*, *56*(69), 235–244. https://doi.org/10.3189/2015AoG69A717

Casey, J. A., Howell, S. E. L., Tivy, A., & Haas, C. (2016). Separability of sea ice types from wide swath C- and L-band synthetic aperture radar imagery acquired during the melt season. *Remote Sensing of Environment*, *174*, 314–328. https://doi.org/10.1016/j.rse.2015.12.021

Cuny, J., Rhines, P. B., & Ron, K. (2005). Davis Strait volume, freshwater and heat fluxes. *Deep Sea Research, Part I*, *52*(3), 519–542. https://doi.org/10.1016/j.dsr.2004.10.006

Dierking, W., & Busche, T. (2006). Sea ice monitoring by L-band SAR: An assessment based on literature and comparisons of JERS-1 and ERS-1 imagery. *IEEE Transactions on Geoscience and Remote Sensing*, *44*(4), 957–970. https://doi.org/10.1109/TGRS.2005.861745

Dierking, W., & Dall, J. (2007). Sea-ice deformation state from synthetic aperture radar imagery—Part I: Comparison of C- and L-band and different polarization. *IEEE Transactions on Geoscience and Remote Sensing*, *45*(11), 3610–3622. https://doi.org/10.1109/TGRS.2007.903711

European Space Agency (2007). Chapter 2: Products and algorithms, *Available online at: envisat.esa.int/handbooks/asar/CNTR2.htm*.

Fors, A. S., Brekke, C., Gerland, S., Doulgeris, A. P., & Beckers, J. F. (2016). Late summer Arctic sea ice surface roughness signatures in C-band SAR data. *IEEE Journal of Selected Topics in Applied Earth Observations and Remote Sensing*, *9*(3), 1199–1215. https://doi.org/10.1109/JSTARS.2015.2504384

Haas, C. (2010). Dynamics versus thermodynamics: The sea ice thickness distribution. In D. N. Thomas & G. S. Dieckmann (Eds.), *Sea ice* (pp. 113–151). Oxford: Wiley-Blackwell.

Haas, C., Beckers, J., King, J., Silis, A., Stroeve, J., Wilkinson, J., et al. (2017). Ice and snow thickness variability and change in the high Arctic Ocean observed by in-situ measurements. *Geophysical Research Letters*, *44*, 10,462–10,469. https://doi.org/10.1002/2017GL075434

Haas, C., & Druckenmiller, M. (2009). Ice thickness and roughness measurements. In H. Eicken (Ed.), *Field techniques for sea ice research* (pp. 49–116). Fairbanks: University of Alaska Press.

Haas, C., Hendricks, S., & Doble, M. (2006). Comparison of the sea-ice thickness distribution in the Lincoln Sea and adjacent Arctic Ocean in 2004 and 2005. *Annals of Glaciology*, *44*(1), 247–252. https://doi.org/10.3189/172756406781811781

Haas, C., Hendricks, S., Eicken, H., & Herber, A. (2010). Synoptic airborne thickness surveys reveal state of Arctic sea ice cover. *Geophysical Research Letters*, *37*, L09501. https://doi.org/10.1029/2010GL042652

Haas, C., & Howell, S. E. L. (2015). Ice thickness in the Northwest Passage. *Geophysical Research Letters*, *42*, 7673–7680. https://doi.org/10.1002/2015gl065704

Haas, C., & Jochmann, P. (2003). Continuous EM and ULS thickness profiling in support of ice force measurements. In S. Loeset, B. Bonnemaire, & M. Bjerkas (Eds.), *The proceedings from the 17th International Conference on Port and Ocean Engineering under Arctic Conditions, POAC ´03* (pp. 849–856). Trondheim, Norway: Department of Civil and Transport Engineering, Norwegian University of Sci.

Haas, C., Lobach, J., Hendricks, S., Rabenstein, L., & Pfaffling, A. (2009). Helicopter-borne measurements of sea ice thickness, using a small and lightweight, digital EM system. *Journal of Applied Geophysics*, *67*(3), 234–241. https://doi.org/10.1016/j.jappgeo.2008.05.005

Haas, C., Pfaffling, A., Hendricks, S., Rabenstein, L., Etienne, J.-L., & Rigor, I. (2008). Reduced ice thickness in Arctic transpolar drift favors rapid ice retreat. *Geophysical Research Letters*, *35*, L17501. https://doi.org/10.1029/2008GL034457

Hanson, A. M. (1965). Studies of the mass budget of Arctic pack-ice floes. *Journal of Glaciology*, *5*(41), 701–709. https://doi.org/10.1017/S0022143000018694

Hibler, W. D. (1972). Removal of aircraft altitude variation from laser profiles of the Arctic ice pack. *Journal of Geophysical Research*, *77*(36), 7190–7195. https://doi.org/10.1029/JC077i036p07190

Howell, S. E. L., Laliberté, F., Kwok, R., Derksen, C., & King, J. (2016). Landfast ice thickness in the Canadian Arctic Archipelago from observations and models. *The Cryosphere*, *10*(4), 1463–1475. https://doi.org/10.5194/tc-10-1463-2016

Hwang, B., Wilkinson, J., Maksym, E., Graber, H. C., Schweiger, A., Horvat, C., et al. (2017). Winter-to-summer transition of Arctic sea ice breakup and floe size distribution in the Beaufort Sea. *Elementa Scince of the Anthropocene*, *5*(0). https://doi.org/10.1525/elementa.232

Intergovernmental Panel on Climate Change (2013). Climate change 2013: The physical science basis. In *Contribution of working group I to the fifth assessment report of the Intergovernmental Panel on Climate Change. Rep.*, (pp. 119–1217). Cambridge, United Kingdom and New York, NY, USA: Cambridge University Press.

King, M. D., Closs, J., Wharton, S., & Myers, M. (Eds.) (2004). *EOS data products handbook* (Vol. 1, pp. 261). Revised 2004. Greenbelt, MD: NASA/Goddard Space Flight Center.

Komarov, A. S., & Barber, D. G. (2014). Sea ice motion tracking from sequential dual-polarization RADARSAT-2 images. *IEEE Transactions on Geoscience and Remote Sensing*, *52*(1), 121–136. https://doi.org/10.1109/TGRS.2012.2236845

Kovacs, A., Holladay, J. S., & Bergeron, C. J. (1995). The footprint/altitude ratio for helicopter electromagnetic sounding of sea-ice thickness: Comparison of theoretical and field estimates. *Geophysics*, *60*(2), 374–380. https://doi.org/10.1190/1.1443773

Kwok, R. (2005). Variability of Nares Strait ice flux. *Geophysical Research Letters*, *32*, L24502. https://doi.org/10.1029/2005GL024768

Kwok, R. (2010). Satellite remote sensing of sea-ice thickness and kinematics: A review. *Journal of Glaciology*, *56*(200), 1129–1140. https://doi.org/10.3189/002214311796406167

Kwok, R. (2015). Sea ice convergence along the Arctic coasts of Greenland and the Canadian Arctic Archipelago: Variability and extremes (1992–2014). *Geophysical Research Letters*, *42*, 7598–7605. https://doi.org/10.1002/2015GL065462

Kwok, R., Cunningham, G. F., Wensnahan, M., Rigor, I., Zwally, H. J., & Yi, D. (2009). Thinning and volume loss of the Arctic Ocean sea ice cover: 2003–2008. *Journal of Geophysical Research*, *114*(C7), C07005. https://doi.org/10.1029/2009JC005312

Kwok, R., Toudal Pedersen, L., Gudmandsen, P., & Pang, S. (2010). Large sea ice outflow into the Nares Strait in 2007. *Geophysical Research Letters*, *37*, L03502. https://doi.org/10.1029/2009GL041872

Lange, B. A. (2012). Seasonal sea ice thickness variability between Canada and the North Pole, Masters thesis, University of Alberta, doi: https://doi.org/10.7939/R39C6S838

Lange, B. A., Flores, H., Michel, C., Beckers, J. F., Bublitz, A., Casey, J. A., et al. (2017). Pan-Arctic Sea ice-algal chl a biomass and suitable habitat are largely underestimated for multi-year ice. *Global Change Biology*, *23*(11), 4581–4597. https://doi.org/10.1111/gcb.13742

Lange, B. A., Michel, C., Beckers, J. F., Casey, J. A., Flores, H., Hatam, I., et al. (2015). Comparing springtime ice-algal chlorophyll a and physical properties of multi-year and first-year sea ice from the Lincoln Sea. *PLoS One*, *10*(4), e0122418. https://doi.org/10.1371/journal.pone.0122418

Laxon, S. W., Giles, K. A., Ridout, A. L., Wingham, D. J., Willatt, R., Cullen, R., et al. (2013). CryoSat-2 estimates of Arctic sea ice thickness and volume. *Geophysical Research Letters*, *40*, 732–737. https://doi.org/10.1002/grl.50193

Lindsay, R., & Schweiger, A. (2015). Arctic sea ice thickness loss determined using subsurface, aircraft, and satellite observations. *The Cryosphere*, *9*(1), 269–283. https://doi.org/10.5194/tc-9-269-2015

Lindsley, R. D., & Long, D. G. (2010). *Standard BYU ASCAT Land/Ice Image Products* (Rep # MERS 10-02/TR-L130-10.02). Microwave Earth Remote Sensing Lab, Bringham Young University.

Manninen, A. T. (1997). Surface roughness of Baltic sea ice. *Journal of Geophysical Research*, *102*(C1), 1119–1139. https://doi.org/10.1029/96JC02991

Maslanik, J. A., Stroeve, J. C., Fowler, C., & Emery, W. (2011). Distribution and trends in Arctic sea ice age through spring 2011. *Geophysical Research Letters*, *38*, L13502. https://doi.org/10.1029/2011GL047735

Massonnet, F., Fichefet, T., Goosse, H., Bitz, C. M., Philippon-Berthier, G., Holland, M. M., & Barriat, P. Y. (2012). Constraining projections of summer Arctic sea ice. *The Cryosphere*, *6*(6), 1383–1394. https://doi.org/10.5194/tc-6-1383-2012

Massonnet, F., Vancoppenolle, M., Goosse, H., Docquier, D., Fichefet, T., & Blanchard-Wrigglesworth, E. (2018). Arctic sea-ice change tied to its mean state through thermodynamic processes. *Nature Climate Change*, *8*(7), 599–603. https://doi.org/10.1038/s41558-018-0204-z

Meier, W. N., Hovelsrud, G., van Oort, B., Key, J., Kovacs, K., Michel, C., et al. (2014). Arctic sea ice in transformation: A review of recent observed changes and impacts on biology and human activity. *Reviews of Geophysics*, *52*, 185–217. https://doi.org/10.1002/2013RG000431

Mortin, J., Howell, S. E. L., Wang, L., Derksen, C., Svensson, G., Graversen, R. G., & Schrøder, T. M. (2014). Extending the QuikSCAT record of seasonal melt–freeze transitions over Arctic sea ice using ASCAT. *Remote Sensing of Environment*, *141*, 214–230. https://doi.org/10.1016/j.rse.2013.11.004

National Aeronautics and Space Administration (2012). *Earth observing system: Mission profiles*. In P. Przyborski (Ed.). Greenbelt, MD, USA: National Aeronautics and Space Administration.

Nicolaus, M., Katlein, C., Maslanik, J., & Hendricks, S. (2012). Changes in Arctic sea ice result in increasing light transmittance and absorption. *Geophysical Research Letters*, *39*, L24501. https://doi.org/10.1029/2012GL053738

Notz, D. (2015). How well must climate models agree with observations? *Philosophical Transactions. Series A, Mathematical, Physical, and Engineering Sciences*, *373*(2052), 20140164. https://doi.org/10.1098/rsta.2014.0164

Ohmura, A. (2012). Present status and variations in the Arctic energy balance. *Polar Science*, *6*(1), 5–13. https://doi.org/10.1016/j.polar.2012.03.003

Parkinson, C. L., & Comiso, J. C. (2013). On the 2012 record low Arctic sea ice cover: Combined impact of preconditioning and an August storm. *Geophysical Research Letters*, *40*, 1356–1361. https://doi.org/10.1002/grl.50349

Perovich, D., Richter-Menge, J., Polashenski, C., Elder, B., Arbetter, T., & Brennick, O. (2014). Sea ice mass balance observations from the North Pole Environmental Observatory. *Geophysical Research Letters*, *41*, 2019–2025. https://doi.org/10.1002/2014GL059356

Perovich, D. K., Grenfell, T. C., Richter-Menge, J. A., Light, B., Tucker, W. B. III, & Eicken, H. (2003). Thin and thinner: Sea ice mass balance measurements during SHEBA. *Journal of Geophysical Research*, *108*(C3), 8050. https://doi.org/10.1029/2001JC001079

Perovich, D. K., & Richter-Menge, J. A. (2015). Regional variability in sea ice melt in a changing Arctic. *Philosophical Ttransactions. Series A, Mathematical, Physical, and Engineering Sciences*, *373*(2045), 20140165. https://doi.org/10.1098/rsta.2014.0165

Pfaffling, A., Haas, C., & Reid, J. E. (2007). Direct helicopter EM-Sea-ice thickness inversion assessed with synthetic and field data. *Geophysics*, *72*(4), F127–F137. https://doi.org/10.1190/1.2732551

Prinsenberg, S. (2014). Pack ice thickness measurements in Nares Strait collected with helicopter-borne electromagnetic-laser sensors during August 2013. *Rep*., 37 pp, can. Tech. Rep. Hydrogr. Ocean Sci.

Prinsenberg, S., Holladay, S., & Lee, J. (2002). Measuring ice thickness with EISFlow (TM), a fixed-mounted helicopter electromagnetic-laser system, Paper Presented at the Twelfth International Offshore and Polar Engineering Conference, International Society of Offshore and Polar Engineers, Kitakyushu, Japan.

Rabenstein, L., Hendricks, S., Martin, T., Pfaffhuber, A., & Haas, C. (2010). Thickness and surface-properties of different sea-ice regimes within the Arctic Trans Polar Drift: Data from summers 2001, 2004 and 2007. *Journal of Geophysical Research*, *115*(C12), C12059. https://doi.org/10.1029/2009JC005846

Rasmussen, T. A. S., Kliem, N., & Kaas, E. (2011). The effect of climate change on the sea ice and hydrography in Nares Strait. *Atmosphere-Ocean*, *49*(3), 245–258. https://doi.org/10.1080/07055900.2011.604404

Reid, J. E., Pfaffling, A., & Vrbancich, J. (2006). Airborne electromagnetic footprints in 1D earths. *Geophysics*, *71*(2), G63–G72. https://doi.org/10.1190/1.2187756

Rosenblum, E., & Eisenman, I. (2017). Sea ice trends in climate models only accurate in runs with biased global warming. *Journal of Climate*, *30*(16), 6265–6278. https://doi.org/10.1175/jcli-d-16-0455.1

Rothrock, D. A., Percival, D. B., & Wensnahan, M. (2008). The decline in arctic sea-ice thickness: Separating the spatial, annual, and interannual variability in a quarter century of submarine data. *Journal of Geophysical Research*, *113*(C5), C05003. https://doi.org/10.1029/2007JC004252

Ryan, P. A., & Münchow, A. (2017). Sea ice draft observations in Nares Strait from 2003 to 2012. *Journal of Geophysical Research: Oceans*, *122*, 3057–3080. https://doi.org/10.1002/2016JC011966

von Saldern, C., Haas, C., & Dierking, W. (2006). Parameterization of Arctic sea-ice surface roughness for application in ice type classification. *Annals of Glaciology*, *44*, 224–230. https://doi.org/10.3189/172756406781811411

Stroeve, J., Barrett, A., Serreze, M., & Schweiger, A. (2014). Using records from submarine, aircraft and satellites to evaluate climate model simulations of Arctic sea ice thickness. *The Cryosphere*, *8*(5), 1839–1854. https://doi.org/10.5194/tc-8-1839-2014

Stroeve, J. C., Kattsov, V., Barrett, A., Serreze, M., Pavlova, T., Holland, M., & Meier, W. N. (2012). Trends in Arctic sea ice extent from CMIP5, CMIP3 and observations. *Geophysical Research Letters*, *39*, L16502. https://doi.org/10.1029/2012GL052676

Stroeve, J. C., Markus, T., Boisvert, L., Miller, J., & Barrett, A. (2014). Changes in Arctic melt season and implications for sea ice loss. *Geophysical Research Letters*, *41*, 1216–1225. https://doi.org/10.1002/2013gl058951

Tang, C. C. L., Ross, C. K., Yao, T., Petrie, B., DeTracey, B. M., & Dunlap, E. (2004). The circulation, water masses and sea-ice of Baffin Bay. *Progress in Oceanography*, *63*(4), 183–228. https://doi.org/10.1016/j.pocean.2004.09.005

Thorndike, A. S., Rothrock, D. A., Maykut, G. A., & Colony, R. (1975). Thickness distribution of sea ice. *Journal of Geophysical Research - Oceans and Atmospheres*, *80*(33), 4501–4513. https://doi.org/10.1029/JC080i033p04501

Tschudi, M., Fowler, C., Maslanik, J., Stewart, J., & Meier, W. (2016). EASE-Grid sea ice age, Version 3. Week 18 of years 2009 and 2013. Boulder, Colorado USA. NASA National Snow and Ice Data Center Distributed Active Archive Center. doi: doi:https://doi.org/10.5067/PFSVFZA9Y85G. Accessed 30 Sept 2018., edited.

Untersteiner, N. (1961). On the mass and heat budget of Arctic sea ice. *Meteorology and Atmospheric Physics*, *12*(2), 151–182.

Wadhams, P. (1997). Ice thickness in the Arctic Ocean: The statistical reliability of experimental data. *Journal of Geophysical Research*, *102*(C13), 27,951–27,959. https://doi.org/10.1029/97JC02503

Warren, S. G., Rigor, I. G., Untersteiner, N., Radionov, V. F., Bryazgin, N. N., Aleksandrov, Y. I., & Colony, R. (1999). Snow depth on Arctic Sea ice. *Journal of Climate*, *12*(6), 1814–1829. https://doi.org/10.1175/1520-0442(1999)012<1814:SDOASI>2.0.CO;2